Histone deacetylase inhibition expands cellular proteostasis repertoires to enhance neuronal stress resilience

Caitlin A. Taylor[1,5,#], Maya Maor-Nof[2,3,5,#], Eyal Metzl-Raz[3], Aaron Hidalgo[1], Callista Yee[4], Aaron D. Gitler[3,5,6], Kang Shen[1,4,5*]

Affiliations:

[1]Department of Biology, Stanford University, Stanford, CA 94305, USA

[2]Department of Biology, Technion - Israel Institute of Technology, Haifa, Israel

[3]Department of Genetics, Stanford University School of Medicine, Stanford, CA 94305, USA

[4]Howard Hughes Medical Institute, Stanford University, Stanford, CA 94305, USA

[5]The Phil and Penny Knight Initiative for Brain Resilience, Stanford University, Stanford, CA, 94305 USA

[6]Chan Zuckerberg Biohub - San Francisco, San Francisco, CA, 94158, USA

# equal contribution

* Correspondence: kangshen@stanford.edu

Abstract

Neurons are long-lived, terminally differentiated cells with limited regenerative capacity. Cellular stressors such as endoplasmic reticulum (ER) protein folding stress and membrane trafficking stress accumulate as neurons age and accompany age-dependent neurodegeneration. Current strategies to improve neuronal resilience are focused on using factors to reprogram neurons or targeting specific proteostasis pathways. We discovered a different approach. In an unbiased screen for modifiers of neuronal membrane trafficking defects, we unexpectedly identified a role for histone deacetylases (HDACs) in limiting cellular flexibility in choosing cellular pathways to respond to diverse types of stress. Genetic or pharmacological inactivation of HDACs

resulted in improved neuronal health in response to ER protein folding stress and endosomal membrane trafficking stress in *C. elegans* and mammalian neurons. Surprisingly, HDAC inhibition enabled neurons to activate latent proteostasis pathways tailored to the nature of the individual stress, instead of generalized transcriptional upregulation. These findings shape our understanding of neuronal stress responses and suggest new therapeutic strategies to enhance neuronal resilience.

Introduction

Cells achieve proteostasis through the regulation of protein synthesis, folding and degradation. In neurons, biosynthetic pathways, degradative systems, and membrane trafficking must act in concert to maintain neuronal morphology and function for decades. Dysregulation of proteostasis is a hallmark of aging and contributes to neurodegenerative diseases (Kurtishi et al., 2019). It is not clear whether these changes are the primary drivers of pathology or are evidence of compensatory stress responses, but improving proteostasis has been a major focus of therapeutic development. Hence, it is critical to understand how cells use different pathways to maintain proteostasis.

Many redundant, interconnected molecular pathways have evolved to maintain robust proteostasis in cells (Balch et al., 2008). Eukaryotic cells possess a complex unfolded protein response (UPR) that maintains homeostasis in response to endoplasmic reticulum (ER) stress. The UPR involves three parallel signaling pathways, IRE1, PERK, and ATF6, which detect unfolded proteins in the ER and resolve ER stress by inducing the production of chaperones to improve protein folding and by decreasing protein folding load (Wiseman et al., 2022). Additionally, there is extensive interplay between the UPR and ER-associated degradation (ERAD), which promotes the clearance of misfolded protein in the ER (Wiseman et al., 2022). UPR and ERAD genes show synthetic lethality in yeast (Costanzo et al., 2010; Thibault et al., 2011), arguing that these pathways function in parallel to resolve ER stress. There is also extensive redundancy in the endo-membrane system that controls protein trafficking, distribution, recycling, and degradation (Lippincott-Schwartz et al., 2000). It remains unexplored whether multiple proteostasis pathways are utilized to a similar extent and whether different cell types rely on specific pathways to execute membrane trafficking.

The utilization of functionally redundant proteostasis pathways is a particularly interesting challenge for neurons. Neurons are highly specialized, terminally differentiated cells. Specialized proteostasis pathways are tailored for their complex cellular needs (Winckler et al., 2018). The longevity of neurons is critical for the fitness of the organism, which places a high demand on maintaining a resilient proteostasis system that can function for decades. Thus, neurons must balance the competing

3

needs for specialization and flexibility. Age-dependent transcriptomic changes in proteostasis have been widely reported, and it has been proposed that disrupting proteostasis is a major contributor to age-related neurodegeneration (Sontag et al., 2017). Indeed, hallmarks of ER stress have been reported in many diseases (Hoozemans et al., 2009; Nijholt et al., 2012; Hetz & Saxena, 2017; Singh et al., 2024). But is the ER stress response an adaptive, beneficial response or instead a maladaptive, detrimental response? The relative benefit or cost of different stress responses likely changes with disease progression. Another unexplored question is whether aging or stressed neurons can utilize the full array of redundant proteostasis pathways. There is the potential for continuous feedback between UPR, ERAD, and protein delivery, but it is not clear if individual cell types are effectively able to leverage these mechanisms when their preferred pathways fail. If neurons are indeed limited to developmentally preferred pathways, there may be manipulations that enable neurons to activate additional stress pathways to promote neuronal survival and health.

We sought to address these questions by studying interconnected trafficking pathways during neuronal development. We performed an unbiased genetic screen for modifiers of a *C. elegans* mutation that results in membrane trafficking stress and a severe neuronal dendritic branching defect. Surprisingly, we discovered that mutations in a histone deacetylase complex (HDAC) potently suppressed this phenotype, improving membrane trafficking and dendritic branching in stressed neurons. HDAC inhibition also potently suppressed a severe neuronal defect caused by a second, mechanistically-distinct type of protein-folding stress, demonstrating the benefit of HDAC inhibition for resolving multiple cellular stressors.

Chromatin modification is a powerful mechanism that regulates the cellular transcriptome during development (Seto & Yoshida, 2014) and plays an important role in cellular stress responses (Tian et al., 2016; Bazopoulou et al., 2019). Interestingly, pharmacological or genetic inhibition of HDACs has shown neuroprotective effects in various contexts (Guan et al., 2009; Choong et al., 2016; Suelves et al., 2017; Janczura et al., 2018). Despite these compelling results, little is known about the cellular mechanisms activated by HDAC inhibition to exert this neuroprotective effect.

4

We used transcriptomic profiling, direct cell biological assays and genetic approaches to dissect the neuroprotective mechanisms of HDAC inhibition in *C. elegans* and mammalian neurons. We revealed that, contrary to expectation, the benefit of histone deacetylase inhibition might not come from general transcriptional upregulation but instead from an increase in cellular flexibility that allows neurons to activate alternative neuronal resilience pathways to deal with diverse neuronal stressors.

Results

SIN-3 is a potent modifier of neuronal protein trafficking and dendrite morphogenesis

To explore the molecular pathways utilized by neurons to cope with cellular stress, we focused on the *C. elegans* nociceptive PVD neuron, which displays an elaborate dendritic arbor. The formation of highly ordered dendritic branches in this neuron requires proper trafficking of membrane proteins through the secretory and endosomal systems (Figure 1A) (Heiman & Bülow, 2024). We previously showed that the loss of RAB-10 recycling endosomes results in a dramatic reduction of dendritic branches (Figure 1B-C) (Taylor et al., 2015; Zou et al., 2015). We harnessed this phenotype and performed a forward genetic suppressor screen to identify regulators of membrane trafficking and define factors that improve neuronal resistance to membrane trafficking stress. We mutagenized *rab-10* mutant animals and performed a visual, microscopy-based screen on F2 progeny to identify mutants with restored dendritic arbors. We isolated two suppressor mutants, *wy1123* and *wy1435*, that increased dendritic branch number in the *rab-10* mutant background (Figure S1A-C). We used SNP-mapping and whole-genome sequencing to identify the causal mutations as R1332X and R1217X, which both cause stop codons in the SIN-3 gene (Figure S1A). We tested two additional *sin-3* alleles, a full deletion of the SIN-3 coding region generated by CRISPR-Cas9 (*wy1340*) and an existing deletion allele (*tm1276*) that likely represents a partial loss-of-function. These alleles also suppressed the *rab-10* branch loss phenotype (Figure 1B, S1B). All four alleles of *sin-3* resulted in reduced fertility, consistent with previous reports (Robert et al., 2023). Thus, loss of SIN-3 is sufficient to partially restore the elaborate PVD neuron dendritic arbor in the absence of RAB-10.
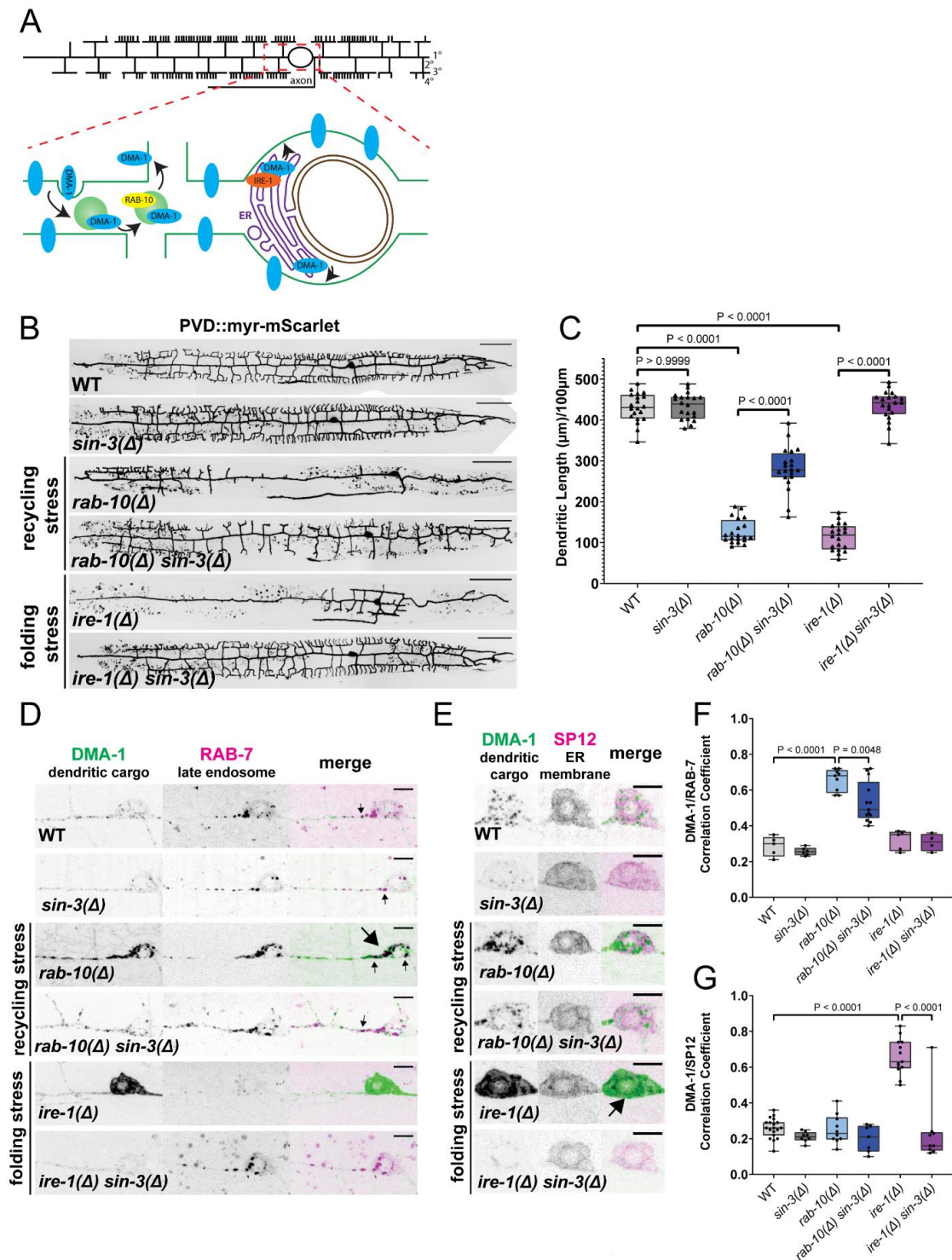
Figure 1. Deletion of sin-3 protects against rab-10 recycling stress and ire-1 folding stress. (A) Schematic of a wild-type PVD dendrite (top) and routes of DMA-1 trafficking in the soma and primary dendrite (bottom). (B) Representative images of PVD morphology in wild-type, *sin-3, rab-10*, and *ire-1* single mutants, and *rab-10, sin-3* and *ire-1, sin-3* double mutants. Scale bars are 50 µm. (C) Quantification of total dendritic length per 100 µm of primary dendrite for genotypes shown in B. (D) Representative images of endogenous DMA-1::GFP and endogenous mScarlet::RAB-7 in PVD somatodendrite region. Scale bars are 5 µm. (E) Representative images of endogenous DMA-1::GFP and endogenous mScarlet::SP12 in PVD soma. Scale bars are 5 µm. (F) Quantification of Pearson's correlation coefficient, indicating degree of co-localization between DMA-1::GFP and mScarlet::RAB-7. (G) Quantification of Pearson's correlation coefficient, indicating degree of co-localization between DMA-1::GFP and mScarlet::SP12. All statistical comparisons were performed using one-way ANOVA with Tukey's correction for multiple comparisons.
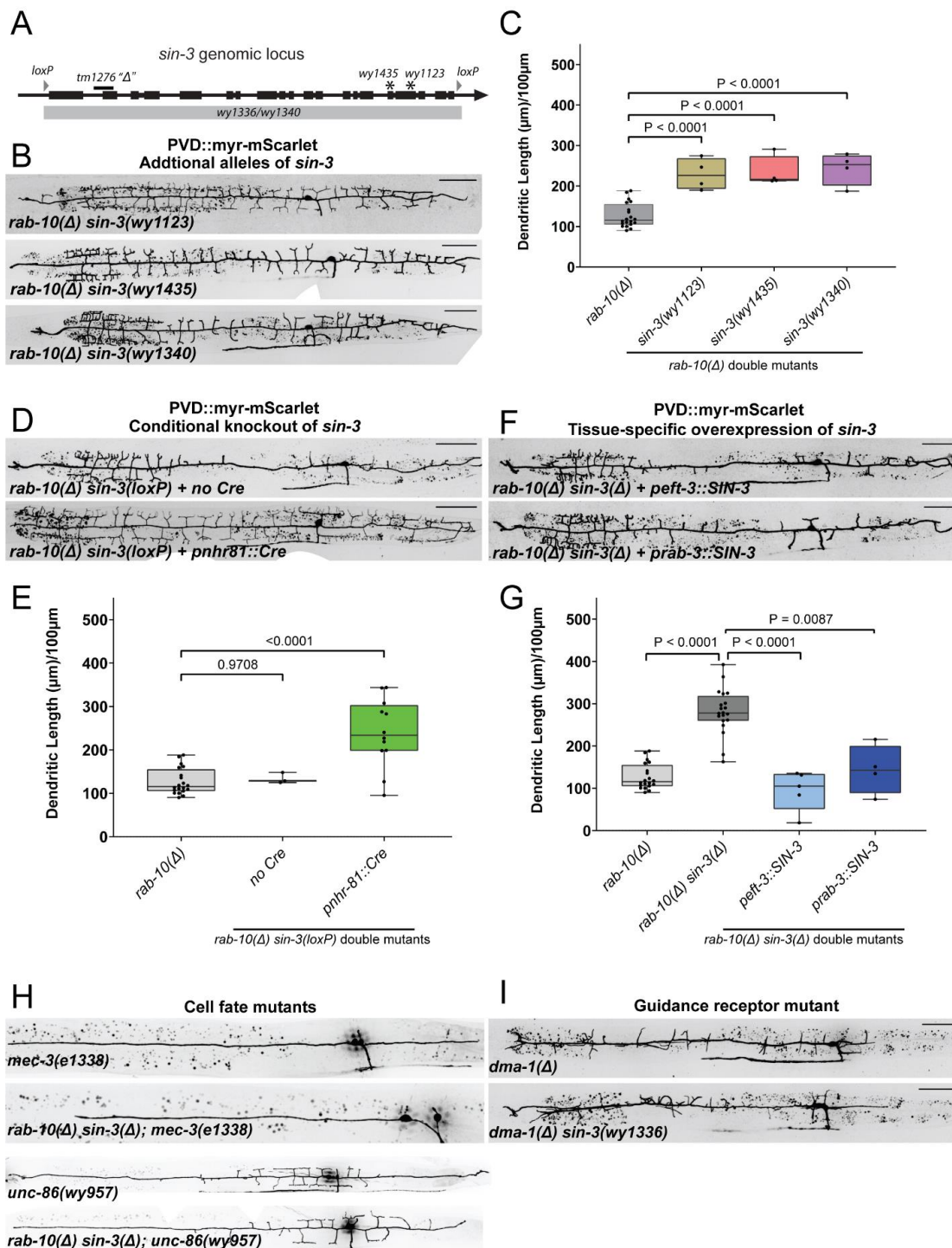
Supplemental Figure 1. SIN-3 functions cell-autonomously in PVD to repress the compensatory growth program. (A) Schematic of the *sin-3* genomic locus depicting all alleles used in this study. (B) Representative images of PVD morphology in double mutants between *rab-10* and three *sin-3* alleles, *wy1123, wy1435*, and *wy1340*. (C) Quantification of total dendritic length per 100 μm of primary dendrite for genotypes shown in B. Quantification of *rab-10* single mutant that first appears in Figure 1C is reproduced here as a control. (D) Representative images of PVD morphology in double mutants of *rab-10* and floxed-*sin-3* with and without Cre. (E) Quantification of total dendritic length per 100 μm of primary dendrite for genotypes shown in D. Quantification of *rab-10* single mutant that first appears in Figure 1C is reproduced here as a control. (F) Representative images of PVD morphology in double mutants of *rab-10* and *sin-3* with single-copy overexpression of SIN-3(cDNA). (G) Quantification of total dendritic length per 100 μm of primary dendrite for genotypes shown in F. Quantification of *rab-10* single mutant and *rab-10, sin-3* double mutant that first appear in Figure 1C are reproduced here as controls. (H) Representative images of PVD morphology in mutants of the transcription factors *mec-3* and *unc-86* with and without the *rab-10* and *sin-3* mutations. (I) Representative images of PVD morphology in mutants of *dma-1* with and without *sin-3* mutation. All statistical comparisons were performed using one-way ANOVA with Tukey's correction for multiple comparisons. All scale bars represent 50 μm.

7

Because of the striking ability of *sin-3* to suppress the *rab-10* dendrite loss phenotype, we next asked if *sin-3* mutations could suppress a neuronal phenotype caused by a different cellular stress. All eukaryotic cells monitor proper protein folding in the endoplasmic reticulum (ER) and respond to ER stress by activating a network of signaling pathways called the unfolded protein response (UPR). Inositol-requiring enzyme (IRE1) is an ER stress sensor essential for the UPR in yeast, plants, and animals. *C. elegans ire-1* mutations cause a severe disruption to the PVD dendritic arbor (Figure 1B) (Wei et al., 2015; Salzberg et al., 2017). Remarkably, *sin-3* mutation was able to completely rescue the *ire-1* dendritic arbor back to wild type (Figure 1B-C). Thus, *sin-3* deficiency potently reversed the severe dendritic branching phenotype elicited by two distinct perturbations (trafficking stress and ER stress).

To define if *sin-3* functions cell autonomously, we performed cell-specific rescue and knockout experiments. Cell specific loss of SIN-3 in the PVD-precursor V5 suppressed the *rab-10* mutant defects (Figure S1D-E). Conversely, upregulation of SIN-3 in all tissues or in only neurons abolished the protective effect of *sin-3* deficiency (Figure S1F-G). Thus, SIN-3 normally functions cell-autonomously in PVD, and the loss of *sin-3* bypasses the requirements for RAB-10 and promotes dendrite growth. We did not observe PVD phenotypes in *sin-3* single mutant animals (Figure 1B), suggesting that SIN-3's function is dispensable during normal development but becomes important upon cellular perturbations such as *rab-10* or *ire-1* deficiency.

Because *sin-3* deficiency was able to rescue strong neuronal phenotypes elicited by distinct cellular stresses, it is axiomatic that *sin-3* must overcome the loss of RAB-10 or IRE-1 function by activating alternative cellular pathways for PVD dendrite branching. We hypothesized that loss of SIN-3 activated a membrane trafficking "backup pathway" that is normally quiescent and is only implemented under stressed conditions. One possibility is that such a "backup pathway" involves a cell-fate change, causing PVD neurons to change their identity and build dendritic arbors using a different set of molecular building blocks. However, loss of the transcription factors *mec-3* or *unc-86*, both of which are required for PVD specification (Way & Chalfie, 1989; Tsalik et al.,

2003; Smith et al., 2010), entirely abolished dendritic arbors in the *sin-3* mutant background (Figure S1H), indicating that *sin-3* mutations do not completely change PVD's cell fate, and the *sin-3* mutant "backup pathway" acts downstream of fate specification by UNC-86/MEC-3.

How does a potential backup pathway resolve two different types of cellular stress and promote dendrite growth? To address this, we next analyzed how *sin-3* rescues the *rab-10* and *ire-1* mutant phenotypes by examining the intracellular trafficking of a key dendrite promoting molecule. DMA-1 is a leucine-rich repeat containing transmembrane protein that promotes dendrite branching and growth in PVD neurons (Liu & Shen, 2011). Deleting *dma-1* abolished dendrites in *sin-3* mutants, suggesting that *sin-3* mutants did not completely alter the molecular program for branching (Figure S1I). Because the DMA-1 guidance receptor is required to build dendrites in both wild-type and *sin-3* mutant animals, we next examined the expression and subcellular localization of DMA-1 in single and double mutants using a previously described endogenous DMA-1::GFP knockin (Eichel et al., 2022). In wild-type animals, DMA-1 showed both diffuse and punctate localization. The majority of punctate DMA-1 co-localized with RAB-10-positive vesicles (Supplemental Movie 1), while the diffuse component likely represents DMA-1 localized to the plasma membrane (Shi et al., 2024). In *rab-10* mutants, DMA-1 was largely missing from the dendrite and abnormally accumulated in the soma and the proximal segment of the primary dendrite in RAB-7-positive compartments (Figure 1D). We quantified the colocalization between DMA-1 and RAB-7 in this somatodendritic domain as a readout of the mistargeting of DMA-1 to the late endosomes. In the *rab-10 sin-3* double mutant, mistargeting of DMA-1 was reduced (Figure 1D, 1F and Supplemental Movie 2). Additionally, the abnormal accumulation of RAB-7 was also reduced, suggesting that *sin-3* is likely to affect trafficking to RAB-7 endosomes rather than specifically regulating DMA-1 (Figure 1D and 1F).

DMA-1 localization was also defective in *ire-1* mutants. However, unlike in *rab-10* mutants, the *ire-1* mutant showed drastically reduced DMA-1 in the dendrite and a strong accumulation in the somatic compartment (Figure 1E). Consistent with IRE-1's function in the UPR, somatic DMA-1 colocalized with the ER marker SP12, suggesting that DMA-1 accumulates in the ER in *ire-1* mutants. We quantified the colocalization

between DMA-1 and SP12 as a readout of the trapping of DMA-1 in ER (Figure 1G). In *ire-1 sin-3* double mutants, this ER-accumulation of DMA-1 was completely resolved (Figure 1E and 1G). Thus, even though *rab-10* and *ire-1* PVD neurons both exhibit dendritic branching defects, the underlying cell biological phenotypes differ, and remarkably *sin-3* deficiency rescues both phenotypes. Together, these data provide evidence that PVD neurons have the capacity to engage alternative protein-processing pathways to resolve diverse membrane trafficking and ER deficits they face, but perplexingly these compensatory pathways can only be utilized in the absence of *sin-3*.

Inhibition of SIN3/HDAC nuclear complex protects against ER stress across biological contexts

SIN-3 is a highly conserved scaffolding and transcriptional corepressor protein that interacts with histone deacetylases (HDACs). SIN-3/HDAC complexes repress gene expression by deacetylating nucleosomes and altering chromatin structure (Seto & Yoshida, 2014). It was surprising that mutations in a transcriptional repressor would have such a profound ability to rescue dramatic neuronal phenotypes. We first asked if SIN-3's effects on PVD dendritic growth depended on HDACs. We tested mutations in six different *C. elegans* HDAC genes and found that loss of only the class I HDAC, *hda-3*, was able to suppress the branching defects of the *ire-1* mutant (Figure 2A-B), suggesting that SIN-3 and HDA-3 function together. We identified two additional conserved components of the SIN-3 complex (ARID-1/ARID4 and ATHP-1/PHF12) whose mutants were also able to suppress the branching defects of *ire-1* mutants (Figure 2A-B), further supporting the notion that SIN-3 and HDA-3 function as a transcriptional repressor complex.
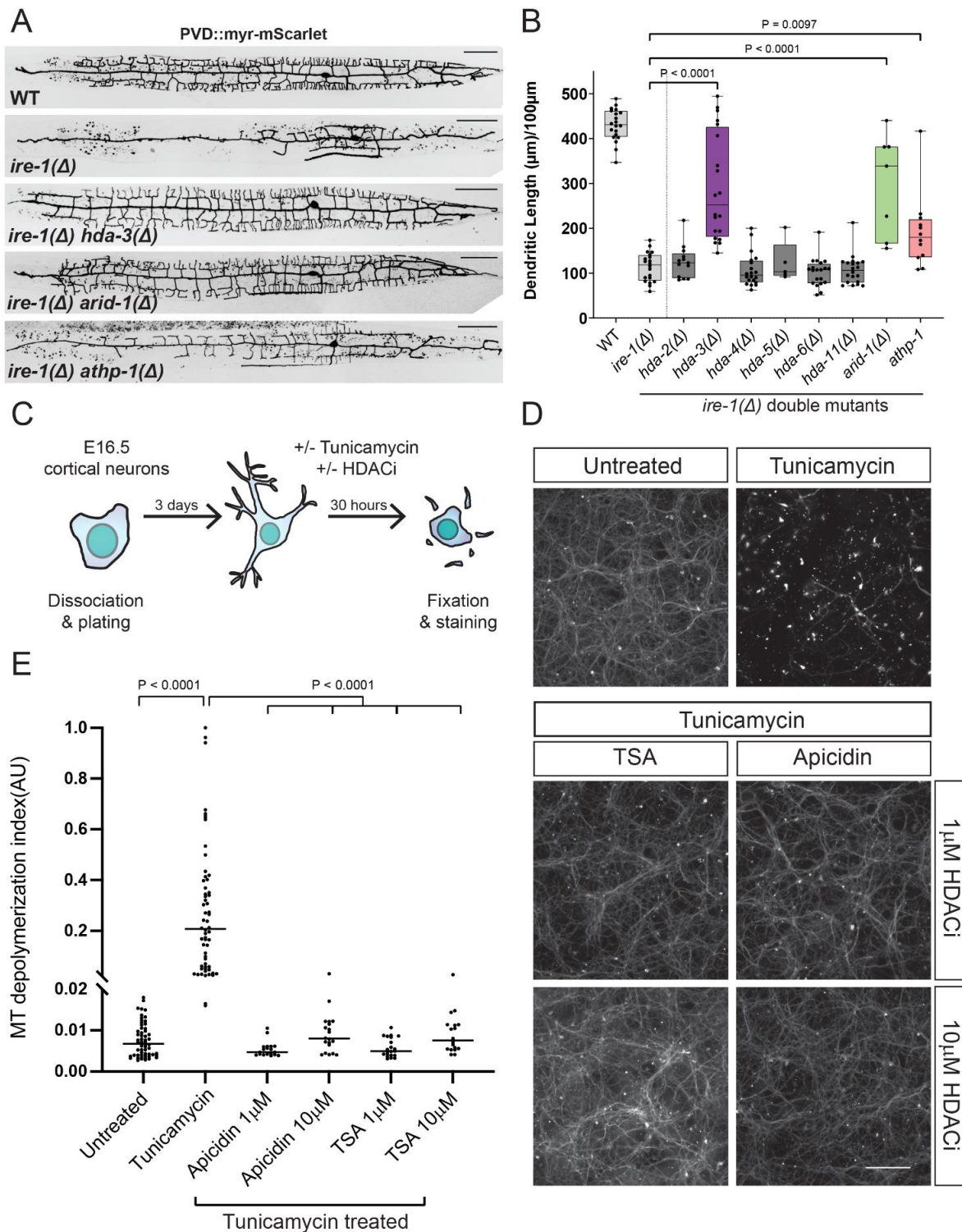
Figure 2. HDAC inhibition protects against ER stress across contexts. (A) Representative images of PVD morphology in wild-type, *ire-1* mutants, and double mutants of *ire-1* with *hda-3, arid-1,* or *athp-1*. Scale bars are 50 μm. (B) Quantification of total dendritic length per 100μm of primary dendrite for genotypes shown in A and additional *hda-* mutants. Statistical comparison was performed using one-way ANOVA with Tukey's correction for multiple comparisons. Wild-type and *ire-1* quantification which first appear in Figure 1C are reproduced here as controls. (C) Schematic of tunicamycin and HDACi treatment of mouse cortical neurons. (D) Representative images of tubulin-βIII staining in mouse cortical neurons treated with or without tunicamycin and with or without apicidin or TSA. Axonal microtubules (MTs) were assessed after treatment. (E) Quantification of microtubule depolymerization index determined from tubulin-βIII staining. Scale bar, 100 μm.
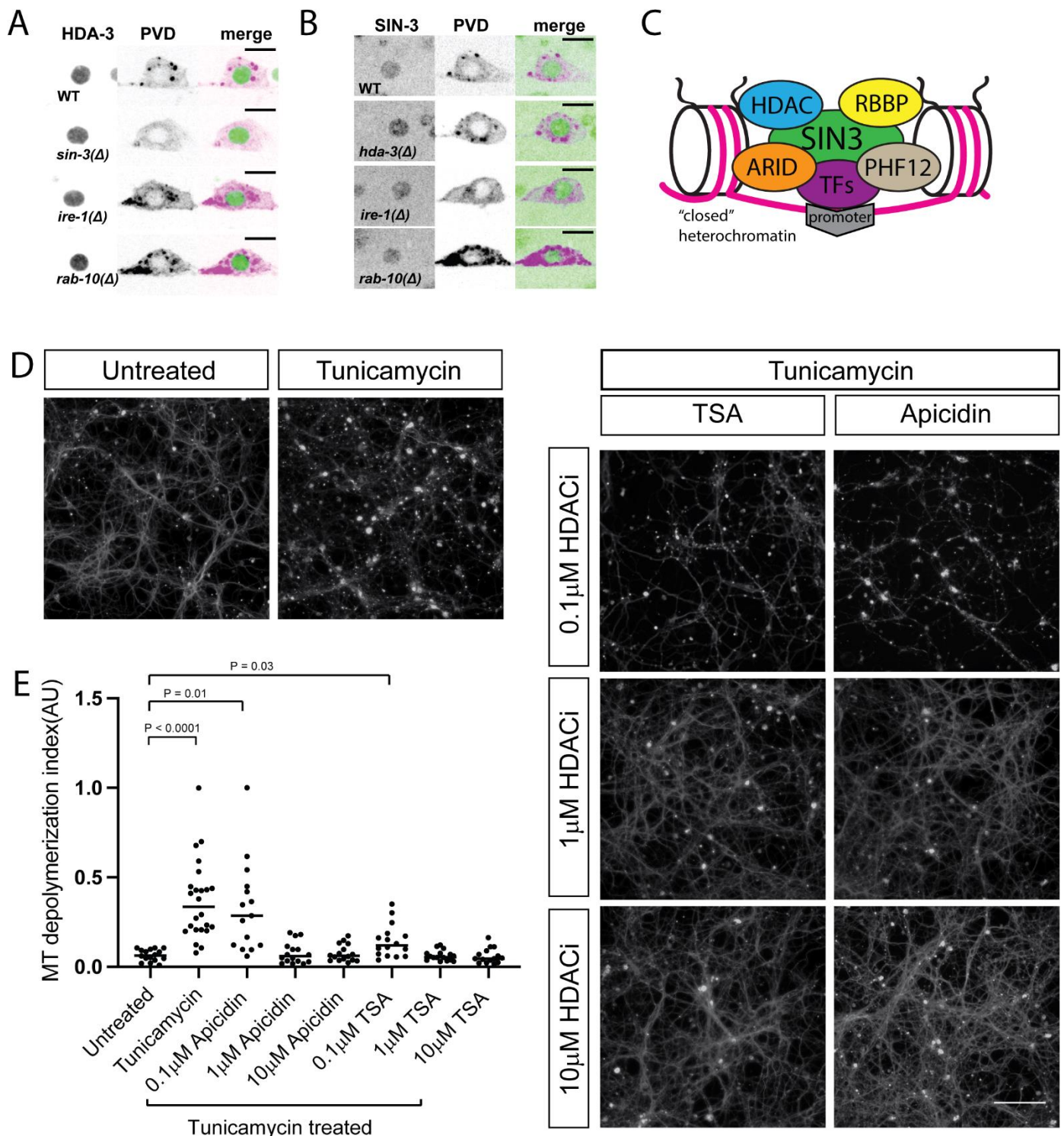
Supplemental Figure 2. HDA-3 and SIN-3 are restricted to the nucleus. (A) Representative images of endogenous HDA-3::GFP with a red membrane marker (pdes-2::mcd8::mScarlet) used to visualize PVD morphology in wild-type, *sin-3, ire-1* and *rab-10* mutants. (B) Representative images of endogenous SIN-3::GFP with a red marker used to visualize PVD morphology in wild-type, *hda-3, ire-1* and *rab-10* mutants. (C) Schematic of potential SIN-3/HDAC complex. (D) Representative images of tubulin-βIII staining in mouse cortical neurons treated with or without tunicamycin and with or without apicidin or TSA. Axonal microtubules (MTs) were assessed after treatment. (E) Quantification of microtubule depolymerization index determined from tubulin-βIII staining. Scale bar, 100 μm.

Most HDAC family members regulate transcription through deacetylating histones, but a few have been shown to work on cytoplasmic proteins such as tubulins (Hubbert et al., 2002; Rivieccio et al., 2009). To test whether SIN-3 and HDA-3 functions in the nucleus, likely to regulate transcription, we examined the subcellular localization of both molecules. We used CRISPR-Cas9 to generate GFP knockins at the endogenous loci for both proteins. SIN-3 and HDA-3 were both constitutively expressed and nuclear-restricted in PVD neurons, indicating that the enzymatic activity of HDA-3 is restricted to the nucleus (Figure S2A-B). The localization of SIN-3 and HDA-3 was unperturbed in *rab-10* and *ire-1* mutants (Figure S2A-B), demonstrating that membrane trafficking stress itself does not change the expression of the SIN-3/HDA-3 complex. Together, these results suggest that a SIN-3/HDA-3 complex acts in the nucleus (Figure S2C), at least in part, to limit the ability of neurons to cope with membrane trafficking or ER stress.

Because of the potent beneficial effect of inhibiting the SIN-3/HDA-3 complex on dendritic arbor formation defects in two different *C. elegans* mutants, we next asked if HDAC inhibitors could protect mature mammalian neurons. We used mouse cortical neurons as a model to examine axonal degeneration in response to ER stress. We cultured E16.5 mouse primary cortical neurons for three days to allow process outgrowth and then treated them with 1μg/mL tunicamycin (Figure 2C). Tunicamycin causes accumulation of unfolded glycoproteins in the ER, leading to ER stress (Oslowski & Urano, 2011). Treatment of mouse cortical neurons with tunicamycin caused numerous tubulin βIII (TUJ1) puncta in the neurites, indicating that microtubules disassembled, and the axons underwent degeneration (Figure 2D-E).

To test whether HDAC inhibition could protect neurons from degeneration, we blocked HDAC activity with two HDAC inhibitors, apicidin and trichostatin A (TSA). TSA affects a wider range of HDAC isoforms, whereas apicidin targets specifically Class I HDACs, which include HDAC1, HDAC2, and HDAC3 (Bradner et al., 2010). We treated neurons with tunicamycin alone or co-treated them with tunicamycin and 1μM and 10μM of TSA or apicidin for 30 hours and stained for tubulin βIII to assess neuronal survival and neurite integrity (Figure 1C). Tunicamycin treatment alone caused strong loss of

neurites, but co-treatment with TSA or apicidin was sufficient to protect neurons from degeneration (Figure 2D-E) in a dose dependent manner (Figure S2D-E). The protective effect conferred by HDAC inhibition was evident for more than 36 hours following ER stress induction. Thus, HDAC inhibition empowers neurons to resist the toxicity of tunicamycin-induced ER stress.

Our genetic data in *C. elegans* and pharmacological experiments in mouse neurons suggest a multifaceted and highly conserved role of HDACs in limiting the ability of neurons to cope with neuronal stressors. Remarkably, it seems that neurons already possess these abilities without needing to be reprogramed or rejuvenated, but they are not permitted to use this ability because of restrictions imposed by HDAC-mediated transcriptional repression. In other words, neurons harbor a network of latent "backup pathway" genes, and when HDACs are inhibited, the restriction on this pathway is relieved and the protective network can be transcriptionally activated.
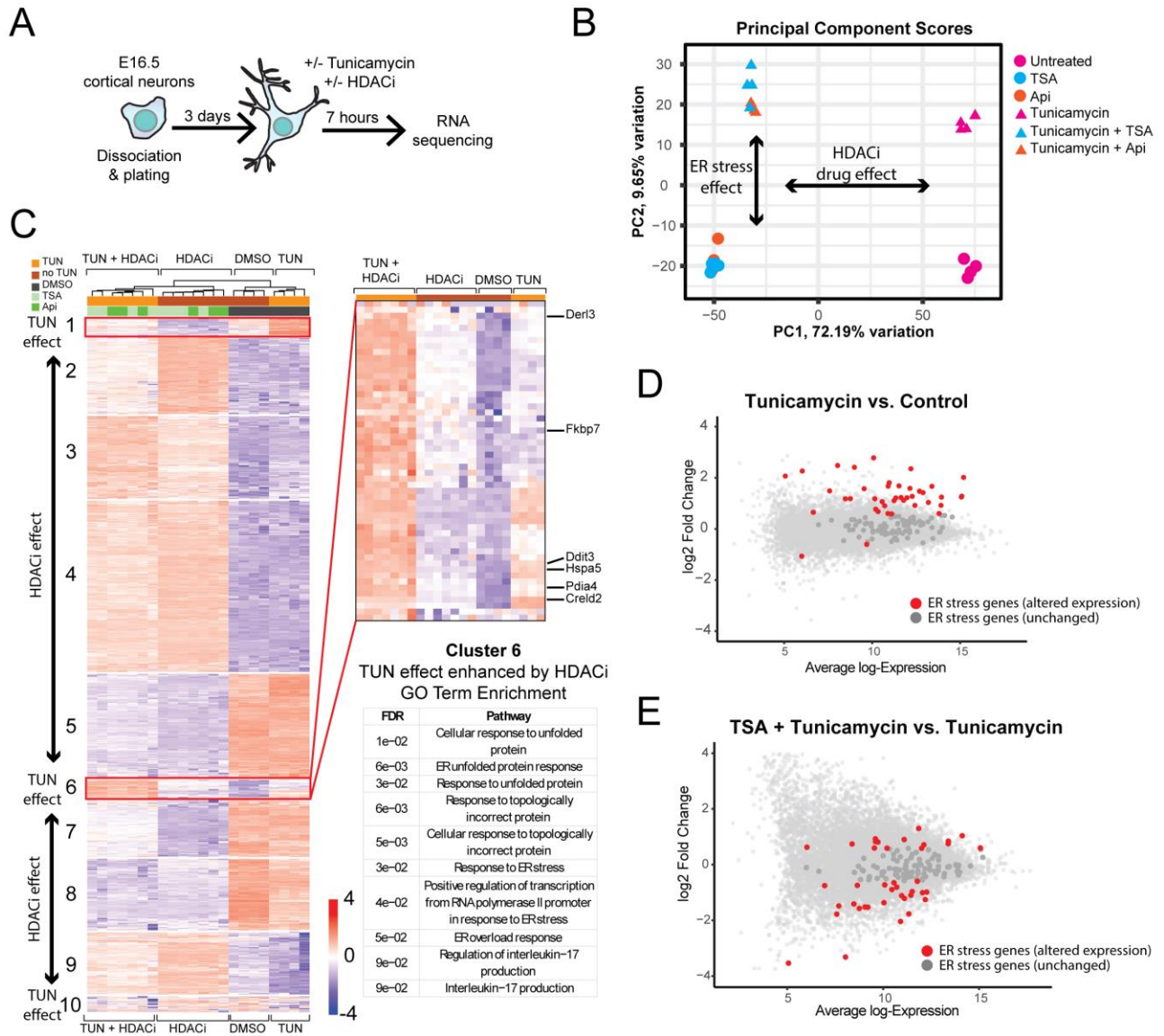
HDAC inhibition regulates a transcriptional response to ER stress in neurons
HDACs play essential roles in the regulation of transcription, cell survival, growth, and proliferation (Seto & Yoshida, 2014). We hypothesized that the protective effect of HDAC inhibition was mediated by a transcriptional program and sought to identify the molecular mechanisms underlying this protection. We first determined the ideal time point after ER stress induction at which to assess the transcriptional programs involved in degeneration or protection. We added HDAC inhibitors at different time points after tunicamycin treatment and assessed the magnitude of axonal degeneration after 24 hours. We found that inhibiting HDACs within 7 hours of tunicamycin treatment provided robust protection against axonal degeneration. To define the transcriptional program unleashed by HDAC inhibition under ER stress, we harvested neurons at 7 hours following tunicamycin treatment with or without the addition of HDAC inhibitors. We extracted RNA and performed RNA sequencing (RNA-seq) (Figure 3A).
RNA-seq measurements revealed a wide array of changes across each treatment (Figure S3A). We used principal component analysis (PCA) to track the differential RNA profiles (Figure 3B), which revealed that the transcriptional changes were primarily explained by two principal components, HDAC inhibitor treatment (PC1) and tunicamycin treatment (PC2). The first principal component (PC1) explained the

greatest possible variance in the sequencing data, reflecting the large number of changes that occur following HDAC inhibition. PC2 explained the second greatest proportion of variance, reflecting the changes that are induced by ER stress. The first two PCs are used for visualization since they capture most of the variation from the dataset (Figure 3B). Notably, we observed very few differentially expressed genes between neurons treated with the two different HDAC inhibitors (Figure S3B), suggesting that the transcriptional program regulated by either TSA or apicidin was highly consistent. To characterize the transcriptional program of HDAC inhibition under ER stress, we first determined the most differentially expressed genes. We found 2000 differently expressed genes that showed high variability between ER stress and HDAC inhibitor treatments. We performed an unsupervised k-means clustering (k=10) analysis to identify different behaviors between the different conditions (tunicamycin +/- HDAC inhibitors). The clustering captured strong changes resulting from HDAC inhibition (clusters 2-5 and 7-9) and tunicamycin treatment (clusters 1,6, and 10) (Figure 3C). Cluster 1 and 6 were notable because they contained genes that were upregulated in response to tunicamycin and this increase in expression was further amplified (Cluster 6) or decreased (Cluster 1) by HDAC inhibition (Figure 3C). Cluster 1 was enriched for genes regulating ER stress; among these were the transcription factor X-Box Binding Protein 1 (Xbp1) and ER stress inducible gene, Tribbles Pseudokinase 3, Trib3. Cluster 6 was enriched for genes related to protein folding, including the ER-associated degradation gene Derl3 and the chaperone Hspa5 (Figure 3C, Figure S3E). We hypothesize that these genes could represent key factors altered by HDAC inhibition that amplify the cell's ability to resolve ER stress.

Consistent with existing literature (Liu et al., 2016; Oslowski & Urano, 2011), we observed a strong increase in signature ER stress genes in tunicamycin treated neurons, including genes functioning in the UPR. KEGG (Kyoto Encyclopedia of Genes and Genomes) pathway analysis revealed "response to endoplasmic reticulum stress" and "response to unfolded protein" to be the most enriched pathways in the gene sets specifically upregulated after tunicamycin treatment (Figure 3C-D, Figure S3C).

Figure 3. HDAC inhibition regulates transcriptional programs that protect against ER stress. (A) Schematic of RNA sequencing experiment performed in mouse cortical neurons. (B) Principal component analysis of all drug treatment groups, displaying PC1 and PC2. (C) K-means clustering, k=10. Highlighted cluster indicates genes upregulated by Tunicamycin and further enhanced by HDAC inhibition. (D) Altered expression of ER stress genes in Tunicamycin vs. control neurons; red indicates ER stress genes with altered expression; dark grey indicates unchanged ER stress genes. (E) ER stress genes in neurons treated with either Tunicamycin and TSA or Tunicamycin alone.

Included in the most highly upregulated genes were protein kinase R-like endoplasmic reticulum kinase (Perk), activating transcription factor 6 (Atf6), activating transcription factor 3 (Atf3), C/EBP Homologous Protein (Chop), Mesencephalic astrocyte derived neurotrophic factor (Manf) as well as Synoviolin 1 (Syvn1) (Figure S3F). Treatment with HDAC inhibitors blunted the overall ER stress transcriptional signature, providing strong

evidence that HDAC inhibition resolves ER stress (Figure 3E). This overall reduction of ER stress genes could be an indirect effect, reflecting the improved handling of ER stress in neurons treated with HDAC inhibition, or it could be a direct effect of HDAC target genes, or a combination of direct and indirect effects. Interestingly, the expression of different subsets of Tunicamycin-induced ER stress genes were shifted in opposite directions upon HDAC inhibition: Cluster 1 was attenuated, and Cluster 6 was enhanced (Figure 3C). Considering HDACs are primarily known for their role in repressing gene activity, we hypothesized that these different groups could represent a split between direct targets of HDAC inhibition (Cluster 6), and indirect transcriptional changes (Cluster 1). Interestingly, while treatment with TSA alone caused many transcriptional changes (Figure S3A), including to ER stress genes, ER stress genes were not among the most highly regulated genes, nor were they coordinately up- or downregulated by TSA alone (FigureS3D).

Taken together, these results suggest that HDAC inhibition transcriptionally modifies the ER stress program that is activated by tunicamycin. However, the transcriptional readout of ER stress does not necessarily indicate functional relevance of individual genes involved in the response ER stress. It is also not clear whether upregulation or downregulation of individual ER stress genes would correspond to beneficial or detrimental effects. To address these questions, we returned to the *C. elegans* PVD neuron to assess the functional importance of ER stress genes in the protective effect of HDAC inhibition.
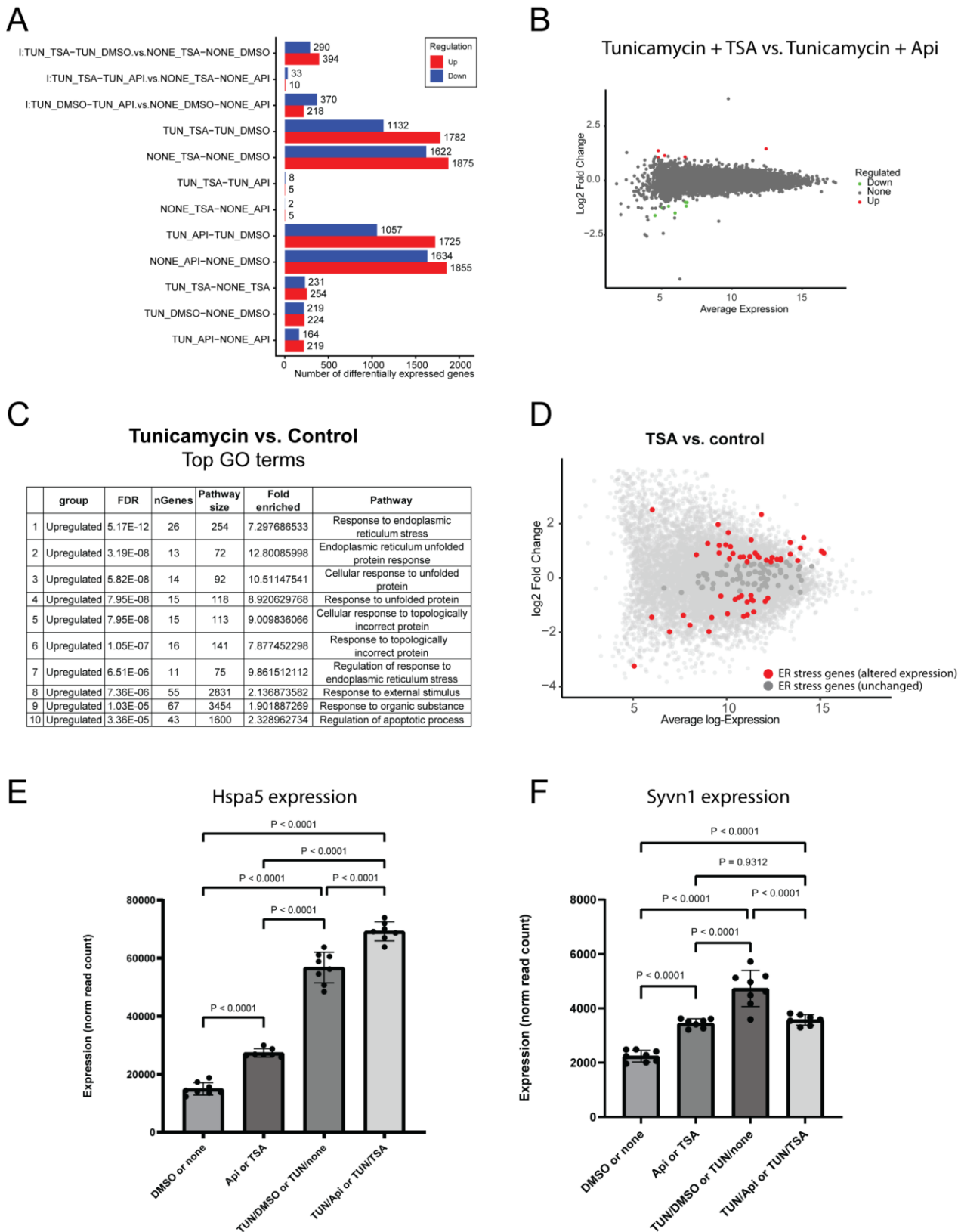
Supplemental Figure 3. Transcriptional regulation of ER stress genes. (A) Total number of differentially expressed genes between conditions. (B) Differentially expressed genes between Tunicamycin and TSA or Apicidin and TSA. (C) GO term enrichment in tunicamycin treated neurons. (D) ER stress genes in TSA compared to control. (E) Expression of Hspa5, a cluster 6 gene that is upregulated by Tunicamycin and enhanced by TSA or apicidin. (F) Expression of Syvn1, an example gene that is upregulated by Tunicamycin and attenuated by TSA or apicidin.

Protective effects of HDAC inhibition rely on ER-associated degradation and protein folding machinery

Because the RNA-seq analysis in mouse primary neurons revealed HDAC inhibition resulted in enhanced expression of ERAD and chaperone gene expression in the face of ER stress (Figure 3C, Cluster 6), we sought to test if genes involved in ERAD were causally responsible for the neuronal protective effect. To do so, we returned to *C. elegans* and used PVD neuron dendritic arborization as a sensitive functional readout of protection. We assembled *C. elegans* orthologs of ERAD genes (Figure S4A) from the mouse neuron RNA-seq and assessed whether each one was required for the protective effect of HDAC inhibition. We constructed triple mutants of *ire-1, sin-3*, and loss-of-function alleles ERAD genes and screened for ones whose loss abolished the protective effect of *sin-3* deletion.

From this analysis, we identified *sel-11*/Syvn1, an ER-localized ubiquitin ligase that degrades misfolded proteins within the ER (Bays et al., 2001) The *ire-1, sin-3*, *sel-11* triple mutant showed a significant reduction in dendritic branches (Figure 4A-B), indicating that ERAD activity is required as part of the protective backup pathway. Several other ubiquitin ligases with different substrate specificities exist in the ERAD system (Christianson et al., 2023). Loss of these other ERAD ubiquitin ligases had no effect (Figure S4A-B), suggesting that degradation of specific sets of ER proteins is required for HDAC inhibition's protective effect. Notably, the ERAD ubiquitin ligase adaptor protein SEL-1/Sel1l was also required for the protective effect; the *ire-1, sin-3, sel-1* triple mutant showed dramatically reduced dendritic branches compared to the *ire-1, sin-3* double mutant (Figure 4A-B). PVD-specific overexpression of SEL-11 or SEL-1 fully restored dendritic branch number in the respective triple mutants, demonstrating that the requirement for ERAD is cell-autonomous (Figure S5A-B and S5D). Importantly, *sel-11* and *sel-1* were entirely dispensable for normal PVD neuron dendritic arborization – *sel-11* or *sel-1* single mutants did not display dendritic defects in an otherwise unstressed background (Figure S4C-D).
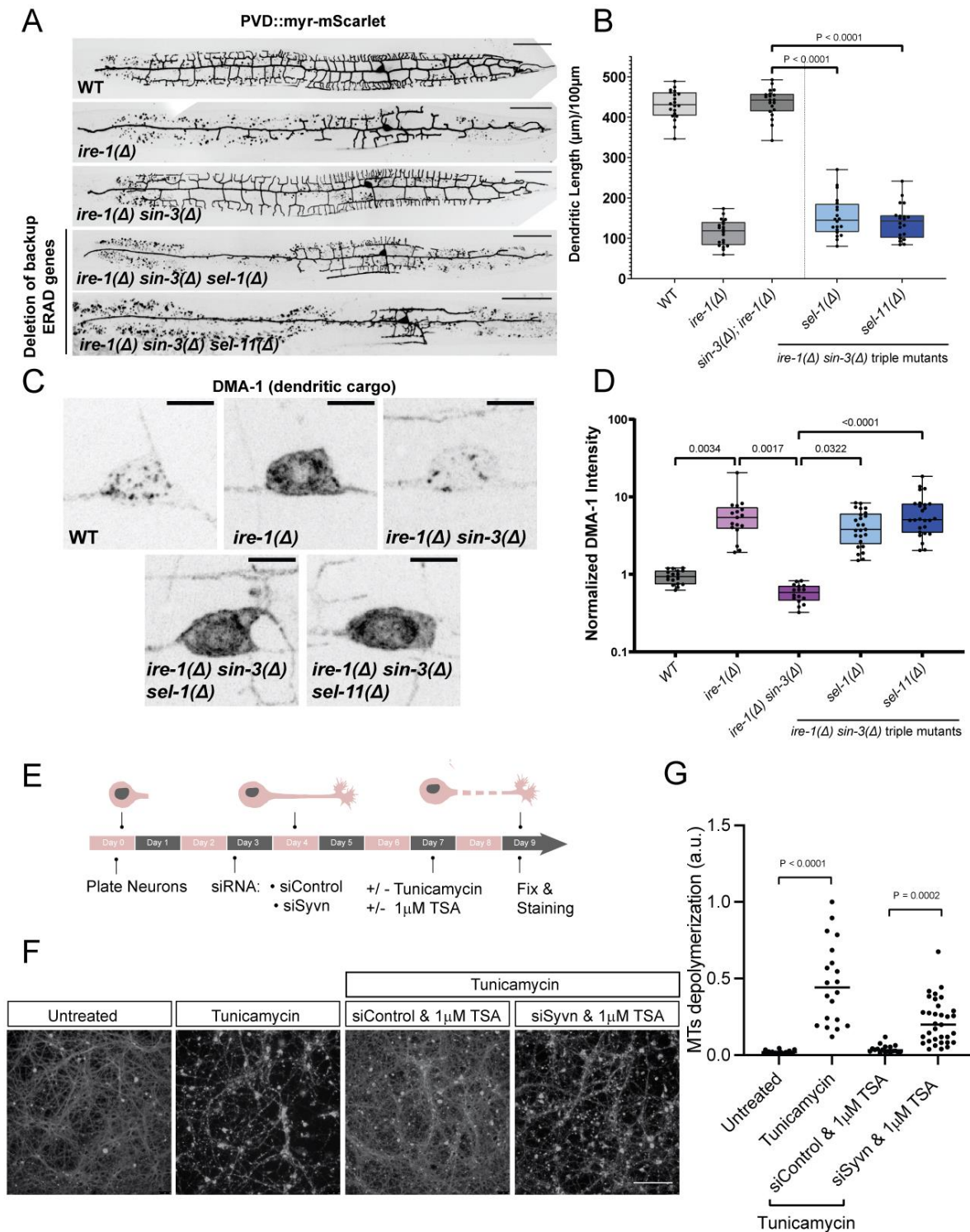
Figure 4. ER-associated degradation (ERAD) is required for the protective effect of HDAC inhibition. (A) Representative images of PVD morphology in triple mutants between *ire-1, sin-3* and the ERAD genes *sel-1* or *sel-11.* Scale bars are 50 µm. (B) Quantification of total dendritic length per 100 µm of primary dendrite for genotypes shown in A. Quantification of wild-type, *ire-1* single mutant, and *ire-1, sin-3* double mutant, which first appear in Figure 1C, are reproduced here as controls. Quantification of the triple mutants is also summarized in the candidate screen shown in S4B. (C) Representative images of endogenous DMA-1::GFP in PVD soma. Scale bars are 5 µm. (D) Quantification of DMA-1::GFP intensity. All genotypes were normalized to the median of wild-type and data are plotted on a log-scale. (E) Schematic of siRNA experiment in mouse cortical neurons. (F) Cortical primary neurons treated with both tunicamycin and TSA after Syvn1 or non-targeting siRNA were added. Axonal microtubules (MTs) were assessed after treatment. (G) Quantification of microtubule depolymerization index determined from tubulin-βIII staining. Scale bar, 100 µm. All statistical comparisons were performed using one-way ANOVA with Tukey's correction for multiple comparisons.

20

Interestingly, overexpression of SEL-1 or SEL-11 in an *ire-1* single mutant was not sufficient to increase branch number (Figure S5C and S5E). This suggests that the protective effect of the *sin-3* deletion cannot be achieved by boosting ERAD alone. This led us to hypothesize that the "backup pathway" comprises multiple components, all of which must be coordinately regulated by HDAC inhibition to achieve the full protective effect. To identify additional factors that were causally responsible for the protective
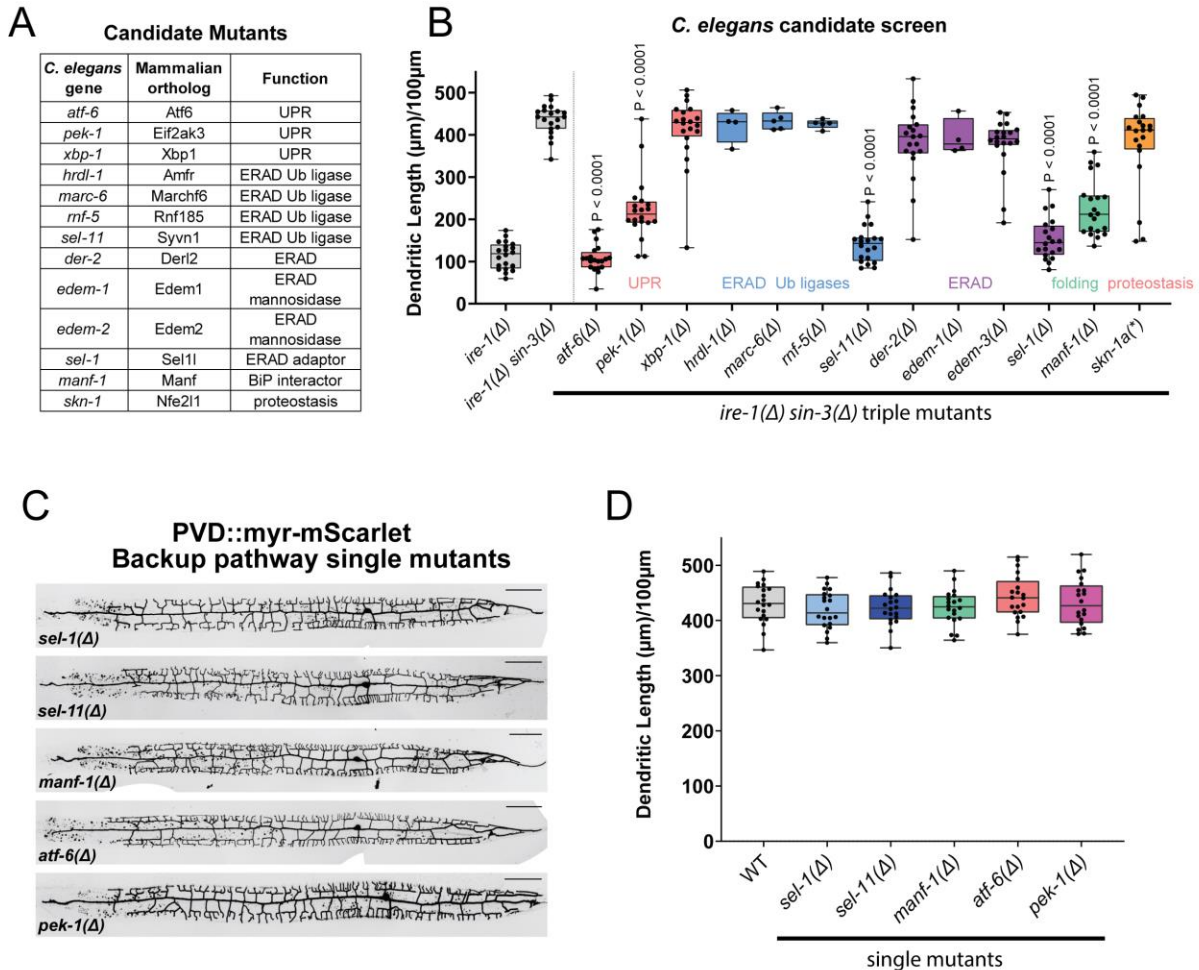
Supplemental Figure 4. Select ERAD and UPR genes are required for the backup pathway. (A) List of candidate mutations tested in *C. elegans* triple mutant screen. (B) Quantification of total dendritic length per 100 µm of primary dendrite for triple mutants between *ire-1, sin-3*, and the listed genotypes. Statistical comparison was performed using one-way ANOVA with Tukey's correction for multiple comparisons. Quantification of *ire-1* single mutant and *ire-1, sin-3* double mutant which first appear in Figure 1C are reproduced here as controls. Triple mutant quantification also appear individually in Figure 4B and 5B. (C) Representative images of PVD morphology in backup pathway single mutants (*sel-1, sel-11, manf-1, atf-6,* and *pek-1*). All scale bars represent 50µm. (D) Quantification of total dendritic length per 100 µm of primary dendrite for genotypes shown in A. Quantification of wild-type which first appears in Figure 1C is reproduced here as a control.

effect, we tested several additional candidate genes involved in protein folding (Figure S4A). We constructed triple mutants of *ire-1*, *sin-3*, and loss-of-function alleles of candidate protein folding genes and identified three additional genes required for the protective effect of *sin-3* deletion: *manf-1, atf-6,* and *pek-1* (Figure S4B, Figure 5A-B). It is interesting to note that these positive hits include both genes whose mammalian orthologs were transcriptionally upregulated upon HDAC inhibition and genes that were transcriptionally downregulated upon HDAC inhibition. This suggests that both direct and indirect targets of HDAC inhibition are functionally relevant for the protective effect and highlights the importance of performing loss-of-function experiments to fully understand the functional significance of transcriptomic data.

The functional requirement for both ERAD and folding genes suggests that the "backup pathway" may rely on both improved folding and clearance of misfolded protein, and we sought to characterize the molecular requirement for both pathways. We performed a series of experiments in *C. elegans* and mouse neurons to characterize the role of both ERAD (Figure 4) and MANF (Figure 5). MANF-1 is the *C. elegans* ortholog of Manf, a neurotrophic factor that protects dopaminergic neurons (Petrova et al., 2003; Lindahl et al., 2017). Manf interacts with the chaperone BiP/Hspa5 and likely contributes to the stabilization of BiP with client proteins (Yan et al., 2019). While *manf-1* single mutants showed no defects in PVD dendritic development (Figure S4C-D), the *ire-1, sin-3,* and *manf-1* triple mutant showed a dramatic reduction in dendritic branches (Figure 5A-B). MANF-1 overexpression rescued this phenotype (Figure S5A-B and S5D), providing evidence that MANF-1 can function cell-autonomously. However, because MANF-1 is secreted, we cannot rule out the possibility that other tissues may contribute to the *manf-1* phenotype. Overexpression of MANF-1 in an *ire-1* single mutant had no positive effect (Figure S5C and S5E), further supporting the idea that the "backup pathway" requires the concerted regulation of multiple pathways, including both ERAD and MANF.

To define how upregulating these alternative pathways by HDAC inhibition helped restore the PVD neuron dendritic arbor in the absence of IRE-1, we examined the localization of DMA-1::GFP. In both the *ire-1, sin-3, sel-1* or *ire-1, sin-3, sel-11* triple mutants, we observed a dramatic accumulation of DMA-1 in the cell body (Figure 4C-

D), which likely represents misfolded, ER-trapped protein that cannot be degraded. *sel-1* or *sel-11* single mutants showed no change in the localization of DMA-1 (Figure S5F-G), again suggesting that ERAD does not play a significant role during the normal processing of DMA-1 under unstressed conditions. DMA-1::GFP localization was also unchanged in a single mutant of *manf-1*, suggesting that MANF-1 is not required for the folding or localization of DMA-1 in unstressed conditions (Figure S5F-G). However, in the *ire-1*, *sin-3*, *manf-1* triple mutant, we observed a strong increase of DMA-1 in the cell body (Figure 5C-D). This suggests that MANF-1 is required for DMA-1 folding and ER exit in the absence of *ire-1*. In the presence of ER stress (i.e., in *ire-1* mutants), neurons could compensate by boosting MANF or ERAD activity but are somehow blocked from doing so. HDAC inhibition releases this block and enables the ERAD pathway to degrade unfolded DMA-1 and MANF to facilitate DMA-1 folding, thus helping to resolve ER stress and enabling dendrite growth and branching.

We next tested if ERAD and MANF are also required for HDAC inhibition's protective effect against ER-stress induced degeneration in mouse neurons. We used small interfering RNA (siRNA) against Syvn1, the mammalian ortholog of *sel-11*, or Manf1, the mammalian ortholog of *manf-1*. We treated primary cortical neurons with either non-targeting siRNA, Syvn1 siRNA, or Manf1 siRNA for 65 hours before the addition of tunicamycin and HDAC inhibitors, TSA and apicidin, for an additional 30h (Figure 4E and 5E). HDAC inhibition conferred protection against axonal degeneration and cell death in ER-stressed neurons treated with a control non-targeting siRNA (Figure 4F-G and 5F-G). In contrast, Syvn1 knockdown markedly attenuated the protective effect (Figure 4F-G). These results suggest that Syvn1 is an important and highly conserved (from worms to mammals) component of the HDAC-inhibition program that mediates resilience to ER-stress induced degeneration. Knockdown of Manf also increased axonal degeneration in neurons treated with both tunicamycin and HDAC inhibitors (Figure 5F-G). This suggests that Manf is also an important part of the backup pathway, similar to Syvn1, and supports the hypothesis that in both *C. elegans* and mouse neurons, both degradation and folding machinery are coordinately regulated as part of the protective pathway activated by HDAC inhibition. We next asked whether additional UPR regulators (*atf-6* and *pek-1)* were required to coordinate this response.

23
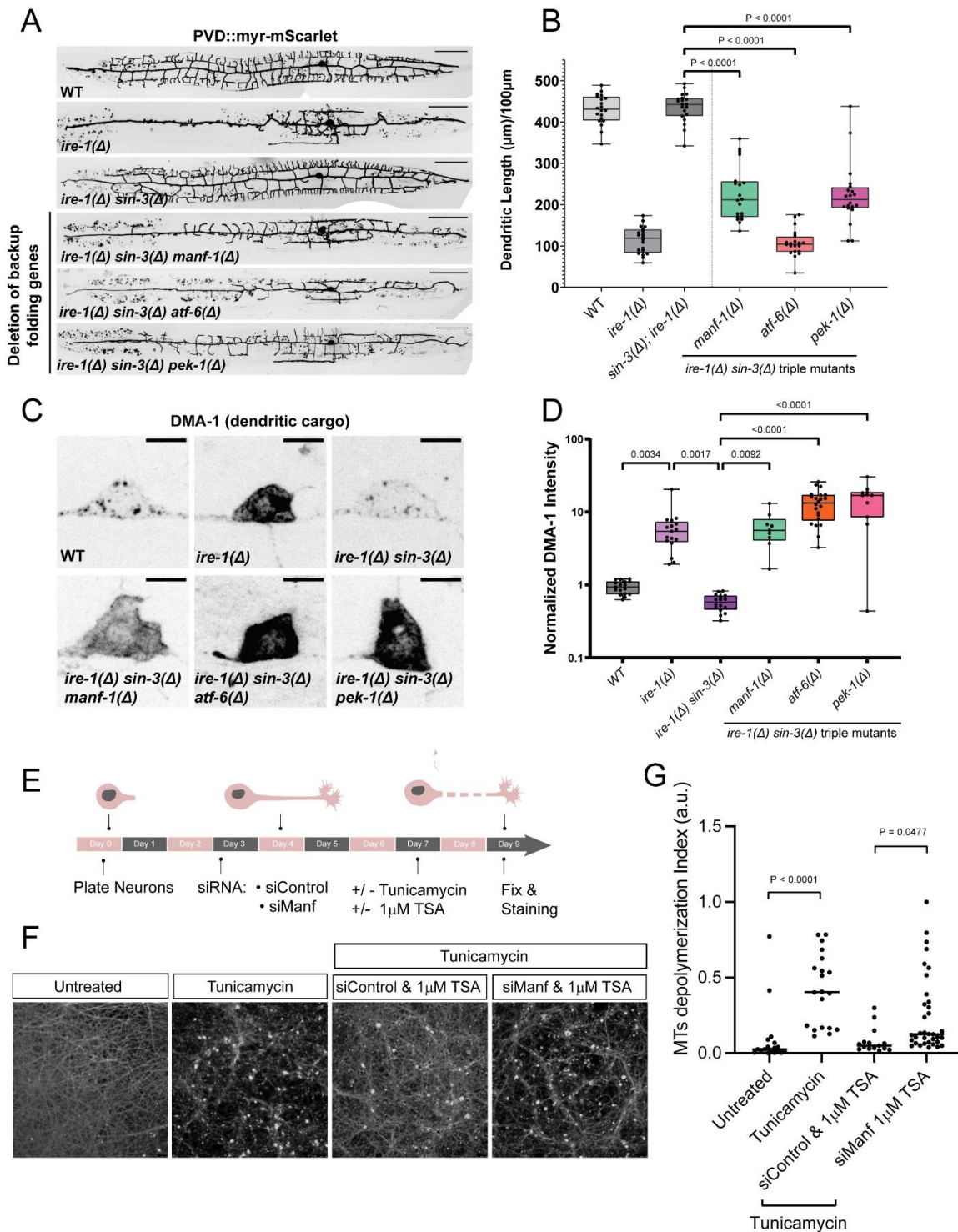
Figure 5. Protein folding components are required for the protective effect of HDAC inhibition. (A) Representative images of PVD morphology in triple mutants between *ire-1, sin-3* and the folding-related genes *manf-1*, *atf-6*, and *pek-1*. Scale bars are 50 µm. (B) Quantification of total dendritic length per 100µm of primary dendrite for genotypes shown in A. Quantification of wild-type, *ire-1* single mutant, and *ire-1, sin-3* double mutant which first appear in Figure 1C are reproduced here as controls. Quantification of the triple mutants is also summarized in the candidate screen shown in S4B. (C) Representative images of endogenous DMA-1::GFP in PVD soma. Scale bars are 5 µm. (D) Quantification of DMA-1::GFP intensity. All genotypes were normalized to the median of wild-type and data are plotted on a log-scale. Quantification of DMA-1::GFP in wild-type, *ire-1* mutant, and *ire-1, sin-3* double mutant which first appear in Figure 4B are repeated here as controls. (E) Schematic of siRNA experiment in mouse cortical neurons. (F) Cortical primary neurons treated with both tunicamycin and TSA after Manf or non-targeting siRNA were added. Axonal microtubules (MTs) were assessed after treatment. (G) Quantification of microtubule depolymerization index determined from tubulin-βIII staining. Scale bar, 100 µm. All statistical comparisons were performed using one-way ANOVA with Tukey's correction for multiple comparisons.

24

Supplemental Figure 5. Multiple components of the backup pathway are required to rescue ER stress phenotypes in PVD. (A) Representative images of PVD morphology in triple mutants of *ire-1, sin-3*, and backup pathway genes (*sel-1, sel-11, manf-1, atf-6,* and *pek-1*). (B) Representative images of PVD morphology in triple mutants of *ire-1, sin-3*, and backup pathway genes (*sel-1, sel-11, manf-1, atf-6,* and *pek-1*) with cell-autonomous rescue constructs. (C) Representative images of PVD morphology in single mutants of *ire-1* with PVD-specific overexpression of backup pathway genes (*sel-1, sel-11, manf-1, atf-6,* and *pek-1*). (D) Quantification of total dendritic length per 100 μm of primary dendrite for genotypes shown in A and B. Quantification of *ire-1, sin-3* single mutant which first appears in Figure 1C is repeated here as a control, and quantification of triple mutants with *ire-1, sin-3* first shown in Figures 4B and 5B (and summarized in Figure S4B) are also shown here as a control. (E) Quantification of total dendritic length per 100 μm of primary dendrite for genotypes shown in C. Quantification of *ire-1* single mutant which first appear in Figure 1C is repeated here as a controls. (F) Representative images of endogenous DMA-1::GFP in backup pathway single mutants (*sel-1, sel-11, manf-1, atf-6,* and *pek-1*). Scale bars are 5 μm. (G) Quantification of DMA-1::GFP intensity. Quantification of DMA-1::GFP in wild-type, *ire-1* single mutant, and *ire-1, sin-3* double mutant which first appear in Figure 4B are repeated here as controls. All statistical comparisons were performed using one-way ANOVA with Tukey's correction for multiple comparisons.

25

In our mini functional screen of ERAD and protein folding genes, *atf-6* was the strongest hit (Figure S4B, Figure 5A-B); *atf-6* mutation completely abolished the ability of *sin-3* to rescue dendritic defects in *ire-1* animals. Mutations in *pek-1* also had an effect, albeit weaker than loss of *atf*-6 (Figure S4B, Figure 5A-B). ATF-6 and PEK-1 are independent arms of the UPR that function in parallel to IRE-1. Consistent with the *ire-1, sin-3, atf-6* and *ire-1, sin-3, pek-1* triple mutants showing a significant reduction in dendritic branching (Figure 5A-B), we observed a strong increase in DMA-1::GFP in the cell body (Figure 5C-D). Intriguingly, under normal conditions, neither *atf-6* nor *pek-1* were required for PVD dendritic arborization (Figure S4C-D) or DMA-1 localization (Figure S5F-G). Overexpression of PEK-1 had no effect on dendrite branching, and overexpression of ATF-6 resulted in a small increase in dendrite branching, which suggests that ATF-6 may be one of the most upstream drivers of the protective effect (Figure S5C and S5E). These data raise the intriguing possibility that both ATF-6 and PEK-1 are required for the folding of DMA-1 under stressed conditions. During normal development, PVD neurons rely heavily upon the IRE-1 arm of the UPR, but not ATF-6 and PEK-1. When this developmentally preferred arm is disabled (i.e., in *ire-1* mutant animals) the cell is incapable of pivoting to the use of ATF-6 and PEK-1 to compensate. And now we have figured out why – because of the repressive effect of HDAC activity. Relieving this repression (by genetic or pharmacological HDAC inhibition) expands the repertoire of available UPR pathways and permits neurons to bring ATF-6 and PEK-1 to bear in the battle to resolve ER stress.

Distinct stressors depend on different compensatory responses

Our data suggest that a network of genes involved in protein folding and degradation, including ERAD, Manf, and the Perk and Atf6 arms of the UPR, are required to protect neurons from ER stress. But are these same genes also required to protect neurons from membrane trafficking stress, which has different underlying cell biological defects? We constructed triple mutants of *rab-10, sin-3* and the ER stress related "backup pathway" genes. Surprisingly, loss of these ER stress backup pathway genes had little effect on the *rab-10, sin-3* double mutant (Figure S6A-B). Loss of ERAD components *sel-1* or *sel-11,* the neuroprotective factor *manf-1*, and loss of UPR gene *pek-1* did not block the ability of *sin-3* to rescue the *rab-10* dendritic branching phenotype, unlike the

26

strong loss of protection we observed in *ire-1, sin-3* mutants. Loss of the UPR regulator *atf-6* caused a small reduction in branches in the *rab-10, sin-3, atf-6* triple mutant, but did not completely abolish the protective effect as it did with *ire-1*. Together, these results suggest that HDAC inhibition rescues the *rab-10* PVD neuron branching phenotype by permitting a different cellular response to be unleashed.
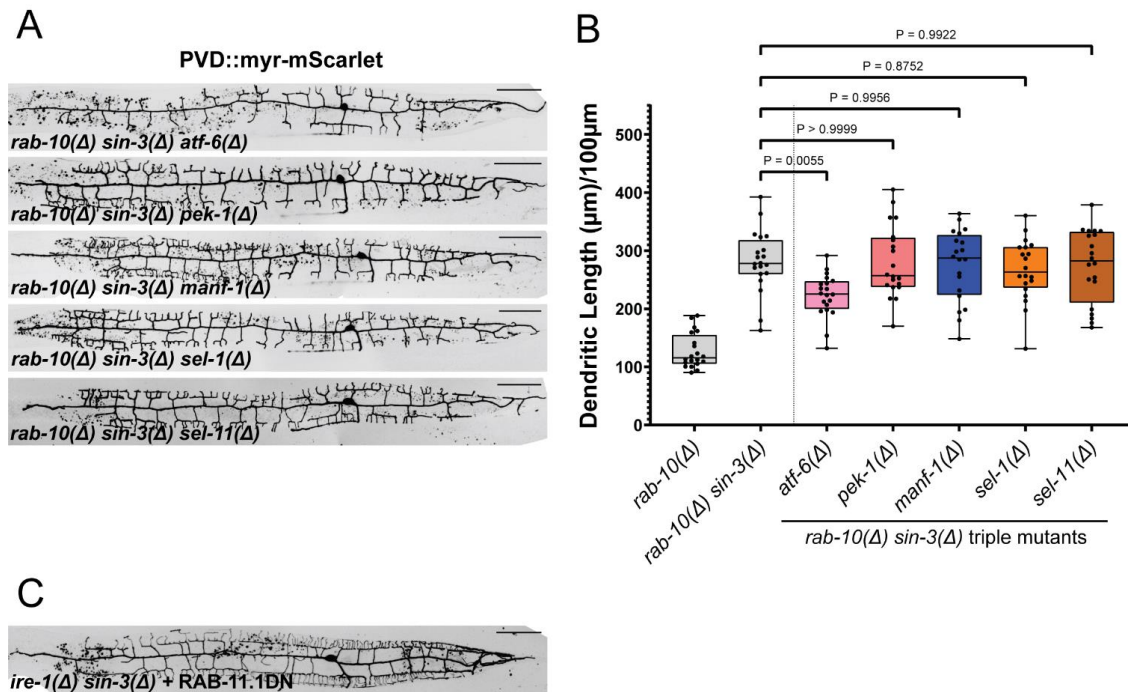

Supplemental Figure 6. Protein folding stress and recycling stress utilize different backup pathways. (A) Representative images of PVD morphology in triple mutants of *rab-10, sin-3*, and ER-stress backup pathway genes (*sel-1, sel-11, manf-1, atf-6,* and *pek-1*). All scale bars represent 50 µm. (B) Quantification of total dendritic length per 100 µm of primary dendrite for genotypes shown in A. Statistical comparison was performed using one-way ANOVA with Tukey's correction for multiple comparisons. Quantification of *rab-10* single mutant and *rab-10, sin-*3 double mutant that first appear in Figure 1C are repeated here as controls. (C) Representative image of PVD morphology in triple mutant of *ire-1, sin-3*, and the endosomal backup pathway gene RAB-11.1(DN).

Activation of alternate endosomes alleviates endosomal recycling stress

We hypothesized that the *sin-3*-deletion backup pathway utilized a distinct cell biological mechanism to correct the trafficking defects observed in *rab-10* mutants (Figure 1D) and sought to identify this alternative protective response and to define the cellular and molecular mechanisms by which *sin-3* deletion promotes growth in *rab-10* mutant neurons. We labeled three different populations of endosomes to monitor membrane trafficking in *rab-10* and *sin-3* mutants.

We visualized early endosomes (RAB-5), late endosomes (RAB-7), and an additional species of recycling endosomes (RAB-11.1) in PVD neurons using cell-specific, endogenous GFP knockins generated by CRISPR-Cas9. In *rab-10* mutants, we observed a depletion of RAB-5 early endosomes (Figure 6A) and an accumulation of both RAB-7 late endosomes and RAB-11.1 endosomes (Figure 6A). We hypothesize that this altered distribution represents an "endosomal traffic jam" – in the absence of the preferred recycling endosome RAB-10, material is mis-sorted. This results in a cascade of dysregulation throughout the interconnected endosomal system, leading to a depletion of RAB-5 early endosomes and an increase in both RAB-7 late endosomes (Supplemental Movie 2) and RAB-11.1 recycling endosomes (Supplemental Movie 3).

The abnormal localization of both RAB-5 early endosomes and RAB-7 late endosomes was rescued in *rab-10, sin-3* double mutants, suggesting that the *sin-3* deletion helped to clear the accumulation of mis-sorted cargos and restore the balance between early and late endosomes (Figure 6A-C). In contrast, the accumulation of RAB-11.1 recycling endosomes was unaffected in *rab-10, sin-3* double mutants (Figure 6A and 6D). We hypothesized that the enhanced function of RAB-11.1 endosomes could represent a potential alternative trafficking pathway unleashed by HDAC inhibition to combat trafficking stress in *rab-10* mutant animals.

To test this hypothesis and functionally validate the role of RAB-11.1 endosomes in supporting branch growth in the absence of *rab-10*, we expressed a dominant-negative form of RAB-11.1 (S25N) in PVD neurons. This had no effect on dendritic branching in wild-type animals (Figure 6E-F) but fully abolished dendritic branches in the *rab-10* mutant, which already had a severe branching phenotype on its own (Figure 6E-F). Inhibiting RAB-11.1 function with the dominant negative construct caused a severe loss of dendritic branches in the *rab-10, sin-3* double mutant (Figure 6E-F), indicating that RAB-11.1 endosomes are required for branch growth. While the abundance of RAB-11.1 endosomes is increased in the *rab-10* single mutant, this increase in RAB-11.1 can only support building a small number of anterior dendrites but is not sufficient to generate a full dendritic arbor (note severe phenotype in the *rab-10* single mutant; Figure 6E). By contrast, when *sin-3* is deleted in *rab-10* mutants, RAB-11.1's role is potentiated, and it becomes capable of partially compensating for the loss of *rab-10*.
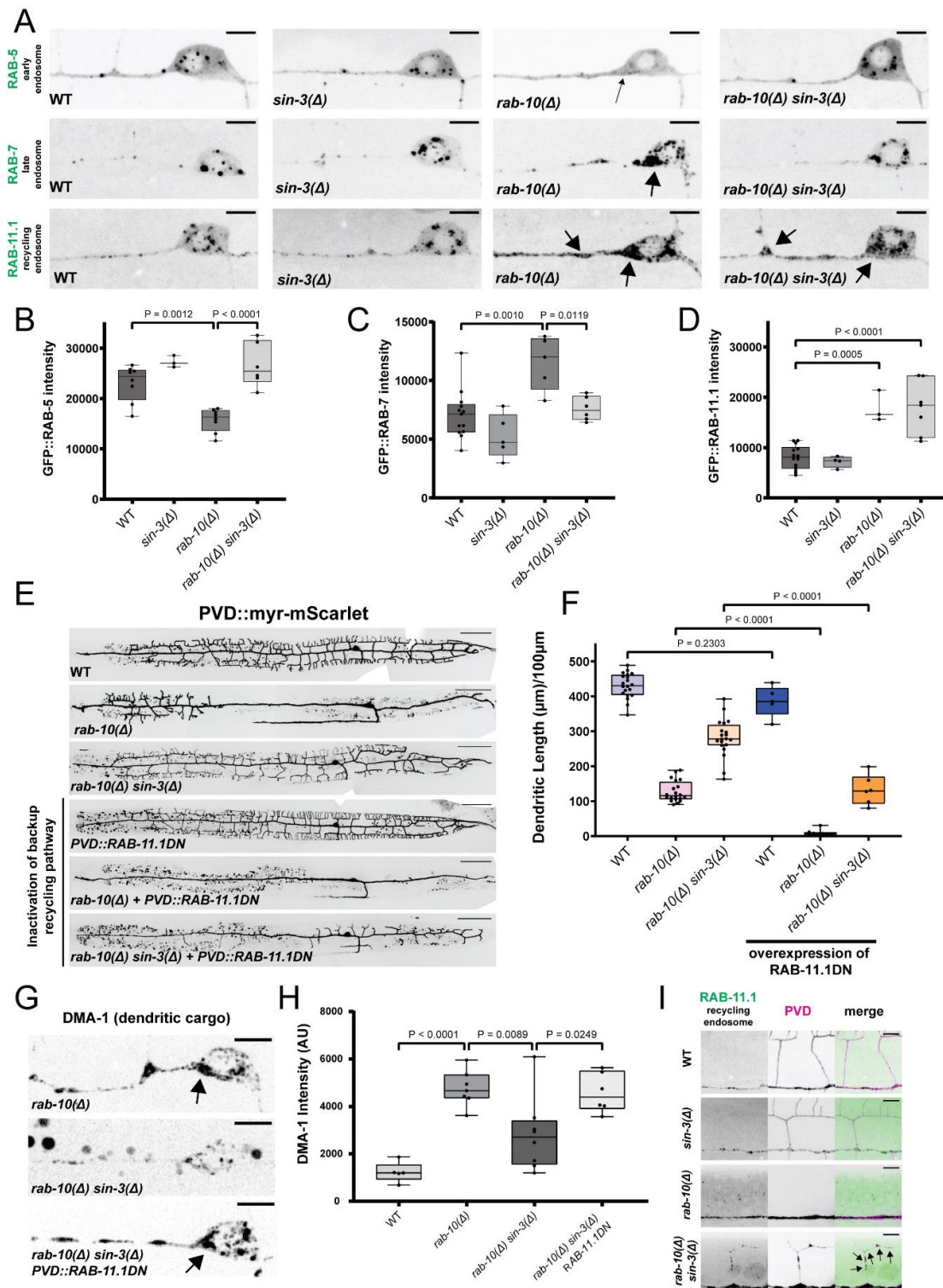
Figure 6. RAB-11.1 recycling endosomes are required for the protective effect of HDAC inhibition. (A) Representative images of endogenous GFP::RAB-5 (top), endogenous GFP::RAB-7 (middle), and endogenous GFP::RAB-11.1 (bottom) in wild-type, *sin-3* and *rab-10* mutants, and *rab-10, sin-3* double mutants. Scale bars are 5 µm. (B) Quantification of GFP::RAB-5 intensity in PVD soma and dendrite for genotypes in A. (C) Quantification of GFP::RAB-7 intensity in the PVD soma and dendrite for genotypes in A. (D) Quantification of GFP::RAB-11.1 intensity in the PVD soma and dendrite for genotypes in A. (E) Representative images of PVD morphology with and without expression of RAB-11.1(DN). Scale bars are 50 µm. (F) Quantification of total dendritic length per 100 µm of primary dendrite for genotypes in D. Quantification of wild-type, *rab-10* mutant, and *rab-10, sin-3* double mutant that first appear in Figure 1C are repeated here as controls. (G) Representative images of endogenous DMA-1::GFP. Scale bars are 5 µm. (H) Quantification of DMA-1::GFP intensity for genotypes in H. (I) Representative images of endogenous GFP::RAB-11.1 localization in higher order dendrites. All statistical comparisons were performed using one-way ANOVA with Tukey's correction for multiple comparisons.

29

To define the mechanism by which RAB-11.1 helps restore dendritic branching, we examined the localization of endogenous DMA-1::GFP. In *rab-10, sin-3*, RAB-11.1(DN) triple mutants, DMA-1 once again accumulated in internal structures in the soma and along the primary dendrite (Figure 6G), resulting in an overall increase in DMA-1 intensity (Figure 6H). This suggests RAB-11.1 may function to recycle or clear DMA-1 in the *rab-10, sin-3* double mutant. We hypothesized that the subcellular localization and movements of RAB-11.1 endosomes could be altered by the loss of *sin-3*. In wild-type animals, we rarely observed RAB-11.1 puncta in the higher-order dendrites (Figure 6I). Instead, RAB-11.1 showed processive movement along the primary dendrite (Supplementary Video 4). In striking contrast, in *rab-10, sin-3* double mutant animals, we observed both stable and dynamic RAB-11.1 puncta in most secondary dendrites (Figure 6I, Supplementary Video 4). This RAB-11.1 behavior recreates the normal dynamics of RAB-10 endosomes in wild-type animals (Supplementary Video 5). Thus, HDAC inhibition empowers RAB-11.1 to substitute for RAB-10. Just as the ER stress backup pathway genes were not required for *sin-3* to rescue the *rab-10* phenotype, RAB11.1 was also dispensable for *sin-3* to rescue the *ire-1* phenotype – in *ire-1*, *sin-3*, and RAB-11.1(DN) triple mutants, dendrites were similar to wild-type controls (Figure S6C). These data provide evidence that RAB11.1 is part of a membrane trafficking backup pathway that can only be fully deployed with the facilitation of HDAC inhibition.

Taken together our data provide evidence that HDAC inhibition provides protection to both protein folding (*ire-1*) and endosomal stress (*rab-10*) by allowing neurons to utilize different downstream pathways in a stress dependent way. Importantly, and perhaps somewhat surprisingly, *sin-3* single mutants showed normal DMA-1 localization (Figure 1E), endosomal localization (Figure 1D, Figure 6A), and a completely normal dendritic arbor (Figure 1B). One expectation might be that inhibiting HDAC activity globally (e.g., in the *sin-3* mutants or in neurons treated with HDAC inhibitors) would lead to widespread upregulation of many different transcriptional programs including protein folding and endosomal genes. While we do see upregulation of numerous targets after HDAC inhibition alone, protein folding genes are notably not enriched. Our RNA-seq results in primary mouse neurons treated with tunicamycin, HDAC inhibitors, or a combination, showed that key ER stress genes were primarily upregulated when cells

were treated with tunicamycin, and selective ER stress programs were further modified (either enhanced or attenuated) after HDAC inhibition. Thus, the protective effect of HDAC inhibition does not result from automatic increases in gene expression, but instead might modify the accessibility of backup gene loci, leaving cells poised to respond to specific stress conditions with alacrity. In other words, it is the nature of the cellular stress which dictates the appropriate backup pathway; HDAC inhibition releases the repressive brake on a broad array of potential cellular countermeasures.

Discussion

Using an unbiased forward genetic screen combined with mechanistic studies and functional validation in worms and mammalian neurons, we uncovered a surprising latent ability of neurons to activate alternative cell biological pathways, which are capable of compensation when preferred growth and neuronal resilience pathways are inactivated. In an otherwise wild-type genetic background, loss of either the unfolded protein response gene *ire-1* or the recycling endosome gene *rab-10* resulted in severe trafficking defects and a greatly reduced capacity to establish complex dendritic branches. Unexpectedly, inhibiting the function of histone deacetylase complexes was sufficient to rescue both these strong phenotypes but did so by allowing the neuron to activate specific pathways suited to the particular cellular stress. This result demonstrates that neurons usually rely on preferred protein and membrane trafficking pathways, which makes them vulnerable. We show that HDAC inhibition expands the repertoires neurons have at their disposal so they can utilize alternative cellular pathways to survive.

HDAC inhibition is beneficial in diverse models of neurodegeneration and neuronal injury (Mai et al., 2009; Shukla & Tekwani, 2020). For example, HDAC inhibitors decreased Aβ plaque number and improved memory impairments in a mouse model of Alzheimer's disease (Guan et al., 2009), blocked neurodegeneration caused by a mutant polyglutamine repeat containing fragment of the Huntington's disease protein (McCampbell et al., 2001), and protected against dopaminergic neuron loss in models of Parkinson's disease (Outeiro et al., 2007). Several potential mechanisms have been proposed, but it is still unresolved how HDAC inhibition provides protection for multiple

cell types in different disease and injury conditions. We found that HDAC inhibition improved neuronal health across species and biological contexts. Genetic ablation of *sin-3* or *hda-3* rescued developmental phenotypes in *C. elegans* neurons facing unfolded protein stress, and pharmacological HDAC inhibition prevented tunicamycin-induced neurodegeneration in mouse cortical neurons. To our knowledge, this is the first demonstration that HDAC inhibition can specifically protect against neuronal ER stress and provides an additional context in which to study the molecular mechanisms of HDAC inhibition. Using these two models of ER stress, we were able to define the underlying mechanism of the protective effect of HDAC inhibition. HDACs can and do regulate many targets, which has made it difficult to identify specific transcriptional changes that underlie the beneficial effects of HDAC inhibition. However, by using loss-of-function analyses we were able to identify transcriptional changes in key pathways, including ER-associated degradation and protein folding that are required for the protective effects of HDAC inhibition.

Interestingly, the relevant HDAC targets were context dependent and differed depending on the particular cellular stress. ERAD genes and MANF were essential to rescue neuronal defects caused by ER stress, but these same pathways were not required for the rescue of endosomal stress. Instead, we found that the protective effect against endosomal stress relied on the activation of alternative vesicle recycling pathways. This endosomal pathway was in turn not required to protect against ER stress. This suggests that the beneficial effect of HDAC inhibition may not be limited to the activation of specific target genes, but rather may result from increased transcriptional flexibility and suggests that that chromatin remodeling is a rate-limiting step in a neuron's ability to respond to these stressors.

It is plausible that the access to latent proteostasis and metabolic pathways might provide widespread protection in different disease insults and injury conditions. This new perspective warrants a re-evaluation of the beneficial effects of HDAC inhibitors across different neurodegenerative disease models to reveal the expanded repertoire of downstream transcriptional programs and signaling pathways that become accessible depending on the specific neuronal insult.

If HDAC inhibition improves cell survival and functionality and equips neurons to respond at will to distinct sources of stress, why do organisms maintain HDACs in the first place? The expanded functional plasticity afforded by HDAC inhibition may come at a cost. Indeed, *sin-3* mutant animals are sterile, owing to profound germline defects, indicating that HDACs play essential functions during development (Robert et al., 2023), and providing a striking example of antagonistic pleiotropy. Many chromatin modifications have been linked to stress responses and cellular and organismal fitness. For example, activation of the mitochondrial stress response requires the di-methylation of histone H3K9, which silences many genes but also activates protective genes (Tian et al., 2016). Similarly, H3K4me3 level is modulated by reactive oxygen species (ROS) and underlies the benefit of early-life ROS exposure on stress resistance and lifespan (Bazopoulou et al., 2019). Additionally, there are other known examples of pro-degenerative factors that limit the ability of cells to respond to stress. For example, inhibition of the conserved dSarm/Sarm1 molecule dramatically improves axon survival after injury models (Osterloh et al., 2012; Gerdts et al., 2013). Mechanistically, SARM1 triggers axon degeneration locally by NAD+ destruction (Gerdts et al., 2015) and might act as a sensor for metabolic changes that occur after injury, helping decide the fate of the injured axon (Sambashivan & Freeman, 2021). But SARM1 also has an essential function in innate immune signaling and *C. elegans* deficient for the SARM1 ortholog, *tir-1*, are more susceptible to infection (Couillault et al., 2004). Thus, chronic constitutive SARM1 inactivation would be deleterious to an organism whereas acute transient inhibition (perhaps immediately following injury) might be beneficial.

We have identified a mechanism by which neurons improve cellular flexibility to respond to protein trafficking stressors. We show that neurons can bypass misfolded protein stress by utilizing alternative UPR and ERAD genes, and neurons can counteract recycling stress by activating alternative endosomal populations. This cell biological flexibility allows neurons to develop normally despite the loss of preferred trafficking pathways. We hypothesize that this cell biological flexibility is modulated by underlying transcriptional flexibility. We propose that transcriptional flexibility is normally limited during differentiation and development to support cell specialization. Under stressed conditions, this rigid specialization can be detrimental to cells. Increasing transcriptional

flexibility improves the ability of cells to activate alternative protein processing pathways and respond to accumulating stress. Cellular chromatin landscapes change during the aging process. A recent study suggests that chromatin flexibility is reduced in aging neurons (Tan et al., 2023), which may contribute to a decreased ability to utilize "backup" pathways to combat cellular stressors. Accruing evidence for adaptive and maladaptive mechanisms in aging and brain disease suggest that aspects of brain aging may be modifiable (Aron et al., 2022). Thus, increasing transcriptional flexibility through chromatin modification may increase brain resilience. Our findings will hopefully motivate the exploration of additional "backup pathways" that are already present in neurons, but dormant, and can be activated by HDAC inhibition to combat diverse neuronal stressors that accumulate with aging, disease, and injury.

Acknowledgments

Methods

C. elegans maintenance

C. elegans animals were grown on nematode growth media (NGM) plates seeded with OP50 *E. coli.* The wild-type reference strain was N2 Bristol. All experiments were performed at 20°C on L4 animals. Sterile worms were maintained using the hT2 (I;III) or mIn1 (II) balancers and balancer-negative homozygotes were selected for imaging experiments. The *glo-1(zu391) X* background was used for all protein-localization experiments to eliminate autofluorescent gut granules.

The following loss-of-function alleles were used in this study: LGI: *rab-10(ok1494), dma-1(tm5159), sin-3(wy1123), sin-3(wy1435), sin-3(wy1340), sin-3(wy1336), sin-3(wy1241), sin-3(tm1276), hrdl-1(wy1744), marc-6(wy1747), hda-3(ok1991);* LGII: *hda-2(ok1479), ire-1(wy1569), ire-1(wy1951), hda-5(wy1968), hda-10(tm2996)*; LGIII: *xbp-1(tm2482), der-2(tm6098), rnf-5(tm794), unc-86(wy957), athp-1(wy1748)*; LGIV: *manf-1(wy1746), hda-6(tm3436), skn-1(mg570), edem-1(tm5068), mec-3(e1338)*; LGV: *hda-11(tm7128), sel-11(wy1740), sel-1(wy1737), arid-1(wy1749)*; LGX: *edem-3(ok1790), atf-6(ok551), pek-1(ok275), hda-4(ok518), glo-1(zu391)*. Deletion alleles were referred to as "Δ" in the figures and text.

The following tagged alleles were used in this study: LGI: *rab-11.1(wy1389[GFP::FLPon(FRT)::rab-11.1]), rab-11.1(wy1947[mScarlet::FLPon(F3)::rab-11.1]), rab-10(wy1616[mScarlet::FLPon(F3)::rab-10]), rab-10(wy1298[GFP::FLPon(FRT)::rab-10]), dma-1(wy1246[DMA-1::GFP]), dma-1(wy1937[DMA-1::GFP]), sin-3(wy1241[sin-3::GFPnovo2]), rab-5(wy1333[GFP::FLPon(FRT)::rab-5]), spcs-1(wy2004[mScarlet::FLPon(F3)::spcs-1]), hda-3(wy1294[hda-3::GFPnovo2])*; LGII: *rab-7(wy1390[GFP::FLPon(FRT)::rab-7]), rab-7(wy1479[mScarlet::FLPon(F3)::rab-7])*.

The following single-copy transgenes were used in this study: LGI: *bmdSi350[pwrt-2::FLP::P2A::H2B::2xmTurq2]*; LGIII: *wySi984[pdes-2::manf-1(cDNA)], wySi987[pdes-2::sel-1(cDNA)], wySi993[pdes-2::rab-11.1(cDNA, S25N)], wySi1013[pdes-2::sel-11(cDNA)], wySi1049[pdes-2::atf-6(cDNA)], wySi1051[pdes-2::pek-1(cDNA)], wySi1047[prab-3::sin-3(cDNA)], wySi1050[peft-3::sin-3(cDNA)], wySi1018[pnhr-*

81::Cre], LG V: wySi937[pdes-2::FLP], wySi960[pdes-2::mcd8-mScarlet], wysi968[pdes-2::mcd8-mScarlet,pdes-2::FLP], wySi996[FLEx-FRT-myr-mScarlet].

A full list of strains is available in Supplementary Table 1.

C. elegans mutant screen

The *sin-3(wy1123)* and *sin-3(wy1435)* alleles were isolated from an F2 semi-clonal suppressor screen performed in the *rab-10* mutant background. Animals carrying a PVD::GFP transgene and *rab-10* mutation were mutagenized with 50mM ethyl methanesulfonate (EMS). F2 animals were visually screened using a fluorescent compound microscope to identify mutants with restored dendritic branching. Standard SNP-mapping was used to map the location of *wy1123* between +2.3 and +2.88 map units on LGI. Whole genome sequencing was used to identify the causal mutation. The *wy1435* allele failed to complement *wy1123*, and the causal mutation was identified by Sanger sequencing of the *sin-3* locus.

Construct generation and *C. elegans* genome editing

Endogenous genomic modifications were performed by gonadal microinjection of Cas9 (IDT), gRNA (IDT), tracrRNA (IDT), and PCR-generated or oligonucleotide (ThermoFisher) repair templates. Deletion alleles were generated using two flanking gRNAs and single-stranded oligonucleotide repair templates. Point mutations and small insertions were generated using a single gRNA and single-stranded oligonucleotide repair template. Fluorophore insertions were generated using a single gRNA and PCR product generated from pSK or pSM vectors. All constructs were created with isothermal assembly (Gibson) and assembled into empty pSK or pSM vector backbones. Single-copy transgene insertions were generated with PCR products generated from pSK or pSM vectors.

A full list of gRNAs is available in Supplementary Table 2.

C. elegans microscopy

All images were obtained at room temperature in live *C. elegans* animals. L4-stage hermaphrodite animals were anesthetized with 10mM levamisole (Sigma-Aldrich) and

mounted on 4% agarose pads. Fluorescently tagged fusion proteins were imaged using a Plan-Apochromat 100x/1.4 oil NA immersion objective on a Zeiss Axio Observer Z1 microscope equipped with a Yokagawa CSU-X1 spinning disk head, a Hamamatsu EM-CCD digital camera, and controlled by MetaMorph (version 7.8.12.0). PVD dendritic morphology was imaged using a C-Apochromat 40x/.9 NA water immersion objective on a Zeiss Axio Observer Z1 microscope equipped with a Yokogawa CSU-W1 spinning disk unit, a Prime 95B Scientific CMOS camera, and controlled by 3i Slidebook (V6). All image processing and quantification was performed using Fiji. All images were displayed in a standardized orientation.

To measure dendritic arborization, the full PVD dendrite was imaged in each worm. Z-stacks were acquired at 3-4 positions along each worm. Maximum-intensity projections were generated for each stack and all positions were assembled into one image using the Pairwise Stitching function. Morphology images were straightened and rotated. The Fiji plugin SNT was used to trace the PVD dendrite and calculate the total length of both primary and higher order dendrites. The length of higher dendrites per 100µm of primary dendrite was calculated for each worm to normalize to primary dendrite length.

To measure the localization and intensity of fluorescently tagged fusion proteins, z-stacks were acquired at the PVD cell soma and proximal primary dendrite. Images were straightened and rotated as z-stacks, and then maximum-intensity and sum-intensity projections were generated. Intensity measurements were obtained from sum-projections, while max-projections were used as display images. Brightness and contrast were adjusted to show relevant features in display images. All images in each experiment were imaged with the same microscope settings and were processed identically for display.

To measure co-localization, an ROI was drawn around the cell soma (for DMA-1/SP12) or the cell body and soma (for DMA-1/RAB-7) and Pearson's Correlation Coefficient was calculated using the "Coloc 2" Fiji Plugin. All measurements were made on z-stacks, while max-projections were used as display images.

To measure vesicular trafficking, the PVD cell soma and proximal primary dendrite were imaged at a single focal plane. For single color imaging, images were acquired every

200ms, while for two color imaging images were acquired every 600ms. All movies were straightened and rotated for display purposes.

C. elegans statistics and reproducibility

Statistical comparisons were performed in Prism 10 (GraphPad) using one-way ANOVA with Tukey's correction for multiple comparisons. *C. elegans* data were presented in box-and-whiskers plots that display all points, the median, and the maximum and minimum values. Each data point represents a single worm (one biological replicate). All imaging experiments were repeated across at least two independent sessions.

For PVD morphology measurements, each genotype was assessed individually and the resultant data was subsequently included in multiple experiments for comparison purposes. A summary of instances in which a quantification is included in more than one graph is provided below.

The quantification of wild-type PVD (n=20 individual worms across 5 imaging sessions) that appeared in Figure 1C was repeated in Figures 2B, 4B, S4D, 5B, and 6F.

The quantification of *rab-10(Δ)* PVD (n=20 individual worms across 5 imaging sessions) that appeared in Figure 1C was repeated in Figures S2C, S2E, S2G, S6B, and 6F.

The quantification of *rab-10(Δ) sin-3(Δ)* PVD (n=20 individual worms across 5 imaging sessions) that appeared in Figure 1C was repeated in Figures S2G, S6B, and 6F.

The quantification of *ire-1(Δ)* PVD (n=20 individual worms across 6 imaging sessions) that appeared in Figure 1C was repeated in Figures 2B, 4B, S4B, 5B, and S5E.

The quantification of *ire-1(Δ), sin-3(Δ)* PVD (n=20 individual worms across 6 imaging sessions) that appeared in Figure 1C was repeated in Figures 4B, S4B, 5B, and S5D.

Quantification of PVD in triple mutants with *ire-1(Δ)* and *sin-3(Δ)* appear in three graphs: individually in Figure 4A (*sel-1* and *sel-11*) and Figure 5A (*manf-1, atf-6,* and *pek-1)*, summarized with the full candidate screen in Figure S4B, and as controls for PVD rescue experiments in Figure S5D. This includes the following genotypes: *ire-1(Δ),sin-3(Δ), sel-11(Δ),* n=20 individual worms across 4 imaging sessions*; ire-1(Δ),sin-3(Δ), sel-1(Δ),* n=20 individual worms across 5 imaging sessions; *ire-1(Δ),sin-3(Δ), manf-1(Δ),* n=20 individual worms across 4 imaging sessions; *ire-1(Δ),sin-3(Δ),atf-6(Δ),* n=20

individual worms across 7 imaging sessions*; ire-1(Δ),sin-3(Δ) pek-1(Δ),* n=20 individual worms across 5 imaging sessions*.*

For DMA-1::GFP measurements, each genotype was assessed individually and the resultant intensity data was subsequently included in multiple experiments for comparison purposes. The quantification of DMA-1 intensity in wild-type (n=25 individual worms across 3 imaging sessions), *ire-1(Δ)* single mutant (n=17 individual worms across 2 imaging sessions), and *ire-1(Δ), sin-3(Δ)* double mutant (n=16 individual worms across 2 imaging sessions) that appeared in Figure 4D was repeated in Figure 5D and S5G.

Antibodies

For immunofluorescence staining of tubulin, we used antibody against Tubulin β-III (Covance, MRB-435P, 1:1,000 dilution). Alexa-dye-conjugated secondary antibodies (Life Technologies, 1:1,000 dilution) were used.

Mice

Animals were bred and used as approved by the Administrative Panel of Laboratory Animal Care (APLAC) of Stanford University, an institution accredited by the Association for the Assessment and Accreditation of Laboratory Animal Crae (AAALAC). Embryos were harvested from pregnant dams at stage E16.5. Wild-type cultures were generated from C57BL/6 mice.

Primary mouse cortical neurons

Primary mouse cortical neurons were dissociated into single-cell suspensions from E16.5 mouse cortices with a papain dissociation system (Worthington Biochemical Corporation). Neurons were seeded onto poly-L-lysine-coated plates (0.1% (wt/vol)) and grown in Neurobasal medium (Gibco) supplemented with B-27 serum-free supplement (Gibco), GlutaMAX, and penicillin-streptomycin (Gibco) in a humidified incubator at 37°C with 5% CO_2. Half media changes were performed every 4 or 5 days, or as required. Neurons were plated on 12mm glass coverslips (Carolina Biological Supplies cat#633009) in 24-well plates (300,000 cells/well) and in 12-well plates for RNA extraction (450,000 cells/well). For ER stress induction, tunicamycin (Sigma-Aldrich

cat#7765) was added by exchanging the medium for medium containing 1µg/mL tunicamycin, with or without the HDAC inhibitors for 30 hours. The HDAC inhibitors used were 0.1-10 µM Trichostatin A (Sigma-Aldrich cat#T8552) and 0.1-10 µM apidin (Sigma-Aldrich cat#A8851).

siRNA treatment

siRNA oligonucleotide sequences were used to target Syvn1 and Manf (Dharmacon, ON-TARGETplus SMARTpool). For negative controls, a nontarget was used (Dharmacon, ON-TARGETplus Non-Targeting Pool, D-001810). Dissociated cortical neurons were transfected with siRNA 3 days after plating, using the protocol supplied with DharmaFECT 4 (Dharmacon, T-2004-03) and performed as previously described (Maor-Nof et al., 2013) with minor modifications. Briefly, siRNA and the transfection reagent were each diluted separately into NB medium with serum and antibiotics for 5 min; then, the siRNA was added to the medium with the transfection reagent. After an additional 20 min incubation, the transfection reagent siRNA complex was added to the dissociated cells and grown in NB medium without serum and antibiotics. 17 hours later, the transfection reagent was removed by replacing the medium with a complete medium, and the neurons were cultured for an additional 48 hr before treatment with tunicamycin and HDAC inhibitors. The final concentration of the siRNA was 0.1 µM.

RNA-sequencing

RNA was isolated from primary neurons treated for 7 hours with either tunicamycin, tunicamycin and HDAC inhibitors, or left untreated. For RNA extraction and isolation, neurons were lysed in RLT buffer from the QIAGEN RNeasy Plus Micro Kit (QIAGEN), according to the manufacturer's protocol. In brief, cells were lysed, homogenized, and loaded on a genomic DNA (gDNA) eliminator column. After removal of genomic DNA, RNA was purified using RNeasy spin columns. RNA quantity and purity were determined by optical density measurements of OD260/280 and OD230/260 using a NanoDrop spectrophotometer. Structural integrity of the total RNA was assessed with the Agilent 2100 Bioanalyzer using the Agilent Total RNA Nano Chip assay (Agilent Technologies). mRNA libraries were prepared for Illumina paired-end sequencing with an Agilent SureSelect Strand Specific RNA-Seq Library Preparation Kit on an Agilent

Bravo Automated Liquid Handling Platform. Libraries were sequenced on an Illumina NextSeq sequencer.

RNA-sequencing Analysis

Alignment of RNA-sequencing reads to the transcriptome was performed with STAR with ENCODE standard options, and read counts were generated with rsem. All libraries were analyzed using iDEP ((Ge et al., 2018). K-mean clustering was performed with k=10, 2000 top genes. Each gene was then centered (subtract mean) and normalized (divided by SD). GO term enrichment was performed using all pass-filtered genes as background. Differential expression analysis was performed using the limma package. Genes with an FDR > 0.1 and absolute log2(fold change) > 2 were considered as significantly differentially expressed genes.

Axonal Quantification *in vitro*

The images of cortical neurons, immuno-stained for β-tubulin, were binarized such that pixels corresponding to axons converted to white while all other regions converted to black. To perform this binarization and differentiate between axons and background in the images, a localized Otsu threshold was used. The Otsu algorithm searches for a threshold that minimizes the variance sum of two or more populations in an image (Otsu, 1979). This gives an exact threshold below which all pixels are considered background. This threshold was then applied to count the number of pixels corresponding to axons in each figure, which serves as the MTs stability index. A punctuated formation of MTs was evident from the cortical explants' staining; these spots occupy only the higher gray levels in the image and appeared mostly in the Tunicamycin treated, and not in their corresponding untreated neurons. The MT depolymerization index was defined as the ratio of depolymerized axon pixel number to intact axon pixel number. To detect the depolymerized axons, we used an algorithm for counting all the pixels above a certain threshold. To find this threshold, we calculated the probability density function (PDF) of the sum-controlled experiments (untreated neurons), from which the cumulative probability density function (CDF) was extracted. The threshold was set as the value above which there were almost no pixels (less than 0.1%). More than six wells were analyzed for each experimental condition.

Mouse Statistical Methods

Analyses were performed using R, Microsoft Excel or Prism 8 (GraphPad), and graphs were plotted using Microsoft Excel or Prism 8. For comparisons among different treatment groups, pairwise analyses were conducted by one-way ANOVA. Data represent mean ± SEM unless otherwise noted. Significance is indicated at the figure legends.

Supplemental Movie legends

Supplemental Movie 1. DMA-1 localizes to RAB-10 vesicles in wild type PVD.

Representative movie of co-labeled DMA-1::GFP (endogenous knockin) and mScarlet::RAB-10 (endogenous knockin) trafficking in PVD neuron. Two-color images acquired every 600ms.

Supplemental Movie 2. DMA-1 is mis-trafficked to RAB-7 late endosomes.

Representative movies of co-labeled DMA-1::GFP (endogenous knockin) and mScarlet::RAB-7 (endogenous knockin) trafficking in wild type, *rab-10* single mutant, and *rab-10, sin-3* double mutant PVD neurons. Two-color images acquired every 600ms.

Supplemental Movie 3. DMA-1 is mis-trafficked to RAB-11.1 recycling endosomes.

Representative movies of co-labeled DMA-1::GFP (endogenous knockin) and mScarlet::RAB-11.1 (endogenous knockin) trafficking in wild type and *rab-10* single mutant PVD neurons. Two-color images acquired every 600ms.

Supplemental Movie 4. RAB-11.1 trafficking is altered by loss of *rab-10* and *sin-3*.

Representative movies of GFP::RAB-11.1 (endogenous knockin) trafficking in wild type, *sin-3* single mutant, and *rab-10, sin-3* double mutant PVD neurons. Images acquired every 200ms.

Supplemental Movie 5. RAB-10 is trafficked to higher order dendrites.

Representative movie of GFP::RAB-10 (endogenous knockin) trafficking in wild type PVD neuron. Images acquired every 200ms.

Supplementary Table 1. List of *C. elegans* strains used in this study.

Group 1: PVD morphology	
Genotype	**Description**
bmdSi350 I; wySi996 V	wild-type PVD
bmdSi350 sin-3(tm1276) I; wySi996 V	sin-3(Δ) mutant PVD
bmdSi350 rab-10(ok1494) I; wySi996 V	rab-10(Δ) mutant PVD
bmdSi350 I; ire-1(wy1569) II; wySi996 V	ire-1(Δ) mutant PVD
bmdSi350 rab-10(ok1494) sin-3(tm1276) I; wySi996 V	rab-10(Δ) sin-3(Δ) double mutant PVD
bmdSi350 sin-3(tm1276) I; ire-1(wy1569) II; wySi996 V	ire-1(Δ), sin-3(Δ) double mutant PVD
bmdSi350 rab-10(ok1494) sin-3(wy1123) I/hT2 (I;III); wySi996 V	rab-10(Δ), sin-3(wy1123) double mutant PVD
bmdSi350 rab-10(ok1494) sin-3(wy1435) I/hT2 (I;III); wySi996 V	rab-10(Δ), sin-3(wy1435) double mutant PVD
bmdSi350 rab-10(ok1494) sin-3(wy1340) I/hT2 (I;III); wySi996 V	rab-10(Δ), sin-3(wy1340) double mutant PVD
bmdSi350 rab-10(ok1494) sin-3(wy1241) I; wySi996 V	rab-10(Δ), sin-3(loxP) double mutant PVD with no Cre
bmdSi350 rab-10(ok1494) sin-3(wy1241) I; wySi1018; wySi996 V	rab-10(Δ), sin-3(loxP) double mutant PVD with V5 Cre
bmdSi350 rab-10(ok1494) sin-3(tm1276) I; wySi1050 III; wySi996 V	rab-10(Δ) sin-3(Δ) double mutant PVD with pan-tissue SIN-3 overexpression

bmdSi350 rab-10(ok1494) sin-3(tm1276) I; wySi1047 III; wySi996 V	rab-10(Δ) sin-3(Δ) double mutant PVD with pan-neuronal SIN-3 overexpression
bmdSi350 dma-1(tm5159) I; wySi996 V	dma-1(Δ) mutant PVD
bmdSi350 dma-1(tm5159) sin-3(wy1336) I/hT2(I;III); wySi996 V	dma-1(Δ), sin-3(Δ) double mutant PVD
bmdSi350 I; hda-2(ok1479) ire-1(wy1951) II/mIn1 II; wySi996 V	ire-1(Δ), hda-2(Δ) double mutant PVD
bmdSi350 hda-3(ok1991) I; ire-1(wy1569) II; wySi996 V	ire-1(Δ), hda-3(Δ) double mutant PVD
bmdSi350 I; ire-1(wy1569) II/mIn1 II; wySi996 V; hda-4(ok518)X	ire-1(Δ), hda-4(Δ) double mutant PVD
bmdSi350 I; ire-1(wy1569) hda-5(wy1968)/mIn1 II II; wySi996 V	ire-1(Δ), hda-5(Δ) double mutant PVD
bmdSi350 I; ire-1(wy1569) II/mIn1 II; hda-6(tm3436) IV; wySi996 V	ire-1(Δ), hda-6(Δ) double mutant PVD
bmdSi350 I; ire-1(wy1569) hda-10(tm2996) II; wySi996 V	ire-1(Δ), hda-10(Δ) double mutant PVD
bmdSi350 I; ire-1(wy1569) II/mIn1 II; wySi996 hda-11(tm7128) V	ire-1(Δ), hda-11(Δ) double mutant PVD
bmdSi350 I; ire-1(wy1569) II; wySi996 arid-1(wy1749) V	ire-1(Δ), arid-1(Δ) double mutant PVD
bmdSi350 I; ire-1(wy1569) II; athp-1(wy1748) III; wySi996 V	ire-1(Δ), athp-1(Δ) double mutant PVD
bmdSi350 I; wySi996 sel-1(wy1737) V	sel-1(Δ) mutant PVD

bmdSi350 sin-3(tm1276) I; ire-1(wy1569) II/mIn1 II; wySi996 sel-1(wy1737) V	ire-1(Δ), sin-3(Δ), sel-1(Δ) triple mutant PVD
bmdSi350 sin-3(tm1276) I; ire-1(wy1569) II/mIn1 II; wySi987 III; wySi996 sel-1(wy1737) V	ire-1(Δ), sin-3(Δ), sel-1(Δ) triple mutant PVD with PVD-specific SEL-1 overexpression
bmdSi350 I; ire-1(wy1569) II; wySi987 III; wySi996 V	ire-1(Δ) single mutant PVD with PVD-specific SEL-1 overexpression
bmdSi350 I; wySi996 sel-11(wy1740) V	sel-11(Δ) mutant PVD
bmdSi350 sin-3(tm1276) I; ire-1(wy1569) II/mIn1 II; wySi996 sel-11(wy1740) V	ire-1(Δ), sin-3(Δ), sel-11(Δ) triple mutant PVD
bmdSi350 sin-3(tm1276) I; ire-1(wy1569) II/mIn1 II; wySi1013 III; wySi996 sel-11(wy1740) V	ire-1(Δ), sin-3(Δ), sel-11(Δ) triple mutant PVD with PVD-specific SEL-11 overexpression
bmdSi350 I; ire-1(wy1569) II; wySi1013 III; wySi996 V	ire-1(Δ) single mutant PVD with PVD-specific SEL-11 overexpression
bmdSi350 I; manf-1(wy1746) IV; wySi996 V	manf-1(Δ) mutant PVD
bmdSi350 sin-3(tm1276) I; ire-1(wy1569) II/mIn1 II; manf-1(wy1746) IV; wySi996 V	ire-1(Δ), sin-3(Δ), manf-1(Δ) triple mutant PVD
bmdSi350 sin-3(tm1276) I; ire-1(wy1569) II/mIn1 II; wySi984 III; manf-1(wy1746) IV; wySi996 V	ire-1(Δ), sin-3(Δ), manf-1(Δ) triple mutant PVD with PVD-specific MANF-1 overexpression
bmdSi350 I; ire-1(wy1569) II; wySi984 III; wySi996 V	ire-1(Δ) single mutant PVD with PVD-specific MANF-1 overexpression

bmdSi350 I; wySi996 V; atf-6(ok551) X	atf-6(Δ) mutant PVD
bmdSi350 sin-3(tm1276) I; ire-1(wy1569) II/mIn1 II; wySi996 V; atf-6(ok551) X	ire-1(Δ), sin-3(Δ), atf-6(Δ) triple mutant PVD
bmdSi350 sin-3(tm1276) I; ire-1(wy1569) II/mIn1 II; wySi1049 III; wySi996 V; atf-6(ok551) X	ire-1(Δ), sin-3(Δ), atf-6(Δ) triple mutant PVD with PVD-specific ATF-6 overexpression
bmdSi350 I; ire-1(wy1569) II; wySi1049 III; wySi996 V	ire-1(Δ) single mutant PVD with PVD-specific ATF-6 overexpression
bmdSi350 I; wySi996 V; pek-1(ok275) X	pek-1(Δ) mutant PVD
bmdSi350 sin-3(tm1276) I; ire-1(wy1569) II/mIn1 II; wySi996 V; pek-1(ok275) X	ire-1(Δ), sin-3(Δ), pek-1(Δ) triple mutant PVD
bmdSi350 sin-3(tm1276) I; ire-1(wy1569) II/mIn1 II; wySi1051 III; wySi996 V; pek-1(ok275) X	ire-1(Δ), sin-3(Δ), pek-1(Δ) triple mutant PVD with PVD-specific PEK-1 overexpression
bmdSi350 I; ire-1(wy1569) II; wySi1051 III; wySi996 V	ire-1(Δ) single mutant PVD with PVD-specific PEK-1 overexpression
bmdSi350 sin-3(tm1276) I; ire-1(wy1569) II; der-2(tm6098) III; wySi996 V	ire-1(Δ), sin-3(Δ), der-2(Δ) triple mutant PVD
bmdSi350 sin-3(tm1276) I; ire-1(wy1569) II/mIn1 II; wySi996 V; edem-3(ok1790) X	ire-1(Δ), sin-3(Δ), edem-3(Δ) triple mutant PVD
bmdSi350 sin-3(tm1276) I; ire-1(wy1569) II/mIn1 II; skn-1a(mg570) IV; wySi996 V	ire-1(Δ), sin-3(Δ), skn-1a(*) triple mutant PVD
bmdSi350 sin-3(tm1276) I; ire-1(wy1569) II; xbp-1(tm2482) III; wySi996 V	ire-1(Δ), sin-3(Δ), xbp-1(Δ) triple mutant PVD

bmdSi350 sin-3(tm1276) marc-6(wy1747) I; ire-1(wy1569) II; wySi996 V	ire-1(Δ), sin-3(Δ), marc-6(Δ) triple mutant PVD
bmdSi350 sin-3(tm1276) hrdl-1(wy1744) I; ire-1(wy1569) II; wySi996 V	ire-1(Δ), sin-3(Δ), hrdl-1(Δ) triple mutant PVD
bmdSi350 sin-3(tm1276) I; ire-1(wy1569) II; edem-1(tm5069) IV; wySi996 V	ire-1(Δ), sin-3(Δ), edem-1(Δ) triple mutant PVD
bmdSi350 sin-3(tm1276) I; ire-1(wy1569) II; rnf-5(tm794) III; wySi996 V	ire-1(Δ), sin-3(Δ), rnf-5(Δ) triple mutant PVD
bmdSi350 rab-10(ok1494) sin-3(tm1276) I; wySi996 sel-1(wy1737) V	rab-10(Δ) sin-3(Δ), sel-1(Δ) triple mutant PVD
bmdSi350 rab-10(ok1494) sin-3(tm1276) I; wySi996 sel-11(wy1740) V	rab-10(Δ) sin-3(Δ), sel-11(Δ) triple mutant PVD
bmdSi350 rab-10(ok1494) sin-3(tm1276) I; manf-1(wy1746) IV; wySi996 V	rab-10(Δ) sin-3(Δ), manf-1(Δ) triple mutant PVD
bmdSi350 rab-10(ok1494) sin-3(tm1276) I; wySi996 V; pek-1(ok275) X	rab-10(Δ) sin-3(Δ), pek-1(Δ) triple mutant PVD
bmdSi350 rab-10(ok1494) sin-3(tm1276) I; wySi996 V; atf-6(ok551) X	rab-10(Δ) sin-3(Δ), atf-6(Δ) triple mutant PVD
bmdSi350 I; wySi993 III; wySi996 V	PVD-specific overexpression of RAB-11.1[S25N]
bmdSi350 rab-10(ok1494) I; wySi993 III; wySi996 V	rab-10(Δ) mutant PVD with PVD-specific overexpression of RAB-11.1[S25N]

Genotype	Description
bmdSi350 rab-10(ok1494) sin-3(tm1276) I; wySi993 III; wySi996 V	rab-10(Δ) sin-3(Δ) double mutant PVD with PVD-specific overexpression of RAB-11.1[S25N]
bmdSi350 I; ire-1(wy1569) II; wySi993 III; wySi996 V	ire-1(Δ), sin-3(Δ) double mutant PVD with PVD-specific overexpression of RAB-11.1[S25N]

Group 2: DMA-1 expression and localization

Genotype	Description
dma-1(wy1246) I; rab-7(wy1479[mScarlet::FLPon(F3)::rab-7]) II; wySi937 V; glo-1(zu391) X	wild type, DMA-1::GFP/mScarlet::RAB-7
sin-3(tm1276) dma-1(wy1937) I; rab-7(wy1479[mScarlet::FLPon(F3)::rab-7]) II; wySi937 V; glo-1(zu391) X	sin-3(Δ) mutant, DMA-1::GFP/mScarlet::RAB-7
rab-10(ok1494) dma-1(wy1246) I /hT2 (I;III); rab-7(wy1479[mScarlet::FLPon(F3)::rab-7]) II; wySi937 V; glo-1(zu391) X	rab-10(Δ) mutant, DMA-1::GFP/mScarlet::RAB-7
rab-10(ok1494) dma-1(wy1937) sin-3(tm1276) I /hT2 (I;III); rab-7(wy1479[mScarlet::FLPon(F3)::rab-7]) II; wySi937 V; glo-1(zu391) X	rab-10(Δ) sin-3(Δ) double mutant, DMA-1::GFP/mScarlet::RAB-7
dma-1(wy1246) I; ire-1(wy1569) rab-7(wy1479[mScarlet::FLPon(F3)::rab-7])/mIn1 II; wySi937 V; glo-1(zu391) X	ire-1(Δ) mutant, DMA-1::GFP/mScarlet::RAB-7

dma-1(wy1937) sin-3(tm1276) I; ire-1(wy1569) rab-7(wy1479[mScarlet::FLPon(F3)::rab-7])/mIn1 II; wySi937 V; glo-1(zu391) X	ire-1(Δ) sin-3(Δ) double mutant, DMA-1::GFP/mScarlet::RAB-7
dma-1(wy1246[DMA-1::GFP]) spcs-1(wy2004[mScarlet::FLPon(F3)::spcs-1]) I; wySi937 V; glo-1(zu391) X	wild type, DMA-1::GFP/mScarlet::SP12
dma-1(wy1937) sin-3(tm1276) spcs-1(wy2004) I/hT2 (I;III); wySi937 V; glo-1(zu391) X	sin-3(Δ) mutant, DMA-1::GFP/mScarlet::SP12
rab-10(ok1494) dma-1(wy1246) spcs-1(wy2004) I/hT2 (I;III); wySi937 V; glo-1(zu391) X	rab-10(Δ) mutant, DMA-1::GFP/mScarlet::SP12
rab-10(ok1494) dma-1(wy1937) sin-3(tm1276) spcs-1(wy2004) I/hT2 (I;III); wySi937 V; glo-1(zu391) X	rab-10(Δ) sin-3(Δ) double mutant, DMA-1::GFP/mScarlet::SP12
dma-1(wy1246) spcs-1(wy2004); ire-1(wy1569) II/mIn1 II; wySi937 V; glo-1(zu391) X	ire-1(Δ) mutant, DMA-1::GFP/mScarlet::SP12
dma-1(wy1937) sin-3(tm1276) spcs-1(wy2004); ire-1(wy1569) II/mIn1 II; wySi937 V; glo-1(zu391) X	ire-1(Δ) sin-3(Δ) double mutant, DMA-1::GFP/mScarlet::SP12
dma-1(wy1246[DMA-1::GFP]) I; wySi960 V; glo-1(zu391) X	wild type, DMA-1::GFP/ PVD::mcd8::mScarlet
rab-10(ok1494) dma-1(wy1246 [DMA-1::GFP]) I/hT2(I;III); wySi960 V; glo-1(zu391) X	rab-10(Δ) mutant, DMA-1::GFP/ PVD::mcd8::mScarlet
dma-1(wy1246[DMA-1::GFP]) I; ire-1(wy1569) II/mIn1 II; wySi960 V; glo-1(zu391) X	ire-1(Δ) mutant, DMA-1::GFP/ PVD::mcd8::mScarlet
rab-10(ok1494) dma-1(wy1937) sin-3(tm1276) I /hT2 (I;III); wySi960 V; glo-1(zu391) X	rab-10(Δ) sin-3(Δ) double mutant, DMA-1::GFP/ PVD::mcd8::mScarlet

51

dma-1(wy1937) sin-3(tm1276) I; ire-1(wy1569) II/mIn1 II; wySi960 V; glo-1(zu391) X	ire-1(Δ), sin-3(Δ) double mutant, DMA-1::GFP/ PVD::mcd8::mScarlet
dma-1(wy1246) I; wySi960 sel-1(wy1737) V; glo-1(zu391) X	sel-1(Δ) mutant, DMA-1::GFP/ PVD::mcd8::mScarlet
dma-1(wy1937) sin-3(tm1276) I; ire-1(wy1569) II/mIn1 II; wySi960 sel-1(wy1737) V; glo-1(zu391) X	ire-1(Δ), sin-3(Δ), sel-1(Δ) triple mutant, DMA-1::GFP/ PVD::mcd8::mScarlet
dma-1(wy1246) I; wySi960 sel-11(wy1740) V; glo-1(zu391) X	sel-11(Δ) mutant, DMA-1::GFP/ PVD::mcd8::mScarlet
dma-1(wy1937) sin-3(tm1276) I; ire-1(wy1569) II/mIn1 II; wySi960 sel-11(wy1740) V; glo-1(zu391) X	ire-1(Δ), sin-3(Δ), sel-11(Δ) triple mutant, DMA-1::GFP/ PVD::mcd8::mScarlet
dma-1(wy1246[DMA-1::GFP]) I; manf-1(wy1746) IV; wySi960 V; glo-1(zu391) X	manf-1(Δ) mutant, DMA-1::GFP/ PVD::mcd8::mScarlet
dma-1(wy1937) sin-3(tm1276) I; ire-1(wy1569) II/mIn1 II; manf-1(wy1746) IV; wySi960 V; glo-1(zu391) X	ire-1(Δ), sin-3(Δ), manf-1(Δ) triple mutant, DMA-1::GFP/ PVD::mcd8::mScarlet
dma-1(wy1246) I; wySi960 V; glo-1(zu391) atf-6(ok551) X	atf-6(Δ) mutant, DMA-1::GFP/ PVD::mcd8::mScarlet
dma-1(wy1937) sin-3(tm1276) I; ire-1(wy1569) II/mIn1 II; wySi960 V; glo-1(zu391) atf-6(ok551) X	ire-1(Δ), sin-3(Δ), atf-6(Δ) triple mutant, DMA-1::GFP/ PVD::mcd8::mScarlet
dma-1(wy1246[DMA-1::GFP]) I; wySi960 V; glo-1(zu391) pek-1(ok275) X	pek-1(Δ) mutant, DMA-1::GFP/ PVD::mcd8::mScarlet

dma-1(wy1937) sin-3(tm1276) I; ire-1(wy1569) II/mIn1 II; wySi960 V; glo-1(zu391) pek-1(ok275) X	ire-1(Δ), sin-3(Δ), pek-1(Δ) triple mutant, DMA-1::GFP/ PVD::mcd8::mScarlet
rab-10(ok1494) dma-1(wy1937) sin-3(tm1276) I/hT2 I; wySi993 III/hT2 III; wySi960 V; glo-1(zu391) X	rab-10(Δ) sin-3(Δ) double mutant with PVD-specific overexpression of RAB-11.1[S25N], DMA-1::GFP/ PVD::mcd8::mScarlet

Group 3: HDAC complex expression

Genotype	Description
hda-3(wy1294[hda-3::GFPnovo2]) I; wySi960 V; glo-1(zu391) X	wild type, HDA-3::GFP
sin-3(tm1276) hda-3(wy1294[hda-3::GFPnovo2]) I; wySi960 V; glo-1(zu391) X	sin-3(Δ) mutant, HDA-3::GFP
rab-10(ok1494) hda-3(wy1294[hda-3::GFPnovo2]) I/hT2(I;III); wySi960 V; glo-1(zu391) X	rab-10(Δ) mutant, HDA-3::GFP
hda-3(wy1294[hda-3::GFPnovo2]) I; ire-1(wy1569) II/mIn1 II; wySi960 V; glo-1(zu391) X	ire-1(Δ) mutant, HDA-3::GFP
sin-3(wy1401[sin-3::GFPnovo2]) I; wySi960 V; glo-1(zu391) X	wild type, SIN-3::GFP
sin-3(wy1401[sin-3::GFPnovo2]) hda-3(ok1991) I; wySi960 V; glo-1(zu391) X	hda-3(Δ) mutant, SIN-3::GFP
rab-10(ok1494) sin-3(wy1401[sin-3::GFPnovo2]) I/hT2 (I;III); wySi960 V; glo-1(zu391) X	rab-10(Δ) mutant, SIN-3::GFP

sin-3(wy1401[sin-3::GFPnovo2]) I; ire-1(wy1569) II/mIn1 II; wySi960 V; glo-1(zu391) X	ire-1(Δ) mutant, SIN-3::GFP

Group 4: Rab compartment expression

Genotype	Description
rab-5(wy1333[GFP::FLPon(FRT)::rab-5]) I; wySi968 V; glo-1(zu391) X	wild type, GFP::RAB-5/ PVD::mcd8::mScarlet
sin-3(tm1276) rab-5(wy1333[GFP::FLPon(FRT)::rab-5]) I/hT2 (I;III); wySi968 V; glo-1(zu391) X	sin-3(Δ) mutant, GFP::RAB-5/ PVD::mcd8::mScarlet
rab-10(ok1494) rab-5(wy1333[GFP::FLPon(FRT)::rab-5]) I/hT2 (I;III); wySi968 V; glo-1(zu391) X	rab-10(Δ) mutant, GFP::RAB-5/ PVD::mcd8::mScarlet
rab-10(ok1494) sin-3(tm1276) rab-5(wy1333[GFP::FLPon(FRT)::rab-5]) I/hT2 (I;III); wySi968 V; glo-1(zu391) X	rab-10(Δ) sin-3(Δ) double mutant, GFP::RAB-5/ PVD::mcd8::mScarlet
rab-7(wy1390[GFP::FLPon(FRT)::rab-7]) II; wySi968 V; glo-1(zu391) X	wild type, GFP::RAB-7/ PVD::mcd8::mScarlet
sin-3(tm1276) I; rab-7(wy1390[GFP::FLPon(FRT)::rab-7]) II; wySi968 V; glo-1(zu391) X	sin-3(Δ) mutant, GFP::RAB-7/ PVD::mcd8::mScarlet
rab-10(ok1494) I/hT2(I;III); rab-7(wy1390[GFP::FLPon(FRT)::rab-7]) II; wySi968 V; glo-1(zu391) X	rab-10(Δ) mutant, GFP::RAB-7/ PVD::mcd8::mScarlet

rab-10(ok1494) sin-3(tm1276) I/hT2(I;III); rab-7(wy1390[GFP::FLPon(FRT)::rab-7]) II; wySi968 V; glo-1(zu391) X	rab-10(Δ) sin-3(Δ) double mutant, GFP::RAB-7/PVD::mcd8::mScarlet
rab-11.1(wy1389[GFP::FLPon(FRT)::rab-11.1]) I; wySi968 V; glo-1(zu391) X	wild type, GFP::RAB-11.1/ PVD::mcd8::mScarlet
rab-11.1(wy1389) sin-3(tm1276) I/hT2 (I;III); wySi968 V; glo-1(zu391) X	sin-3(Δ) mutant, GFP::RAB-11.1/ PVD::mcd8::mScarlet
rab-11.1(wy1389[GFP::FLPon(FRT)::rab-11.1]) rab-10(ok1494) I/hT2 (I;III); wySi968 V; glo-1(zu391) X	rab-10(Δ) mutant, GFP::RAB-11.1/ PVD::mcd8::mScarlet
rab-11.1(wy1389[GFP::FLPon(FRT)::rab-11.1]) rab-10(ok1494) sin-3(tm1276) I/hT2 (I;III); wySi968 V; glo-1(zu391) X	rab-10(Δ) sin-3(Δ) double mutant, GFP::RAB-11.1/ PVD::mcd8::mScarlet

Supplemental Table 2. List of gRNAs used for CRISPR-Cas9.

Allele	sgRNA	Description
rab-11.1(wy1947)	tacagctcagcagtaaagAT	mScarlet::FLPon(F3)::rab-11.1
dma-1(wy1937)	CTTCGTGAGCGACAGTACAA	internal DMA-1::GFP, identical to wy1246, CRISPR in *sin-3(tm1276)* background
sin-3(wy1336)	ctgaaaggcaaaagcgagag, ctgtagtaggtcaaaagacg	full deletion of *sin-3.* identical to wy1340, CRISPR in *dma-1(tm5159)* background

sin-3(wy1340)	ctgaaaggcaaaagcgagag, ctgtagtaggtcaaaagacg	full deletion of *sin-3*
sin-3(wy1241)	ctgaaaggcaaaagcgagag, ctgtagtaggtcaaaagacg	loxP::sin-3::loxP
sin-3(wy1401)	GCACGATAGCTGATAATTGT	sin-3::GFPnovo2
hrdl-1(wy1744)	tggaatttcagATGAATACG, cttgtcatttcaaagctacc	full deletion of *hrdl-1*
spcs-1(wy2004)	attacataattaaccATGGA	mScarlet::FLPon(F3)::spcs-1
marc-6(wy1747)	ttcagaatcctcaaaccgaA, aaagattcacacggaaaaac	full deletion of *marc-6*
hda-3(wy1294)	GGCGAAAATGTGGCATAAtt	hda-3::GFPnovo2
ire-1(wy1569)	tggtggttgatgacgccccg, aaacatgaggacaagaccat	deletes 2nd half of ire-1 (all exons after *unc-105* locus)
ire-1(wy1951)	tggtggttgatgacgccccg, aaacatgaggacaagaccat	deletes 2nd half of ire-1. identical to wy1569, CRISPR in *hda-2(ok1479)* background
hda-5(wy1968)	cataatcggtcaaacatcag, tagactccatttagactgtc	full deletion of *hda-5* locus by CRISPR
rab-7(wy1479)	cttccagtgaacaaaaATGT	mScarlet::FLPon(F3)::rab-7
athp-1(wy1748)	aatagtatgtgaatcgagga, atcaaaatacgtgatattca	full deletion of *athp-1*

manf-1(wy1746)	CTCATctgctggaaaaaaca, cacgattatcacatgtagaa	full deletion of *manf-1*
sel-11(wy1740)	ATACCCTCATctgaattccg, gacaacgagaaattaattac	full deletion of *sel-11*
sel-1(wy1737)	TAGTAGCAACAGTGTCAGAT, ggaatgtgcttaactgggca	full deletion of *sel-1*
arid-1(wy1749)	gaattgagctggactcgccg, agagtatcgagaaaatgcgt	full deletion of *arid-1*

References

1. Aron, L., Zullo, J., & Yankner, B. A. (2022). The adaptive aging brain. *Current Opinion in Neurobiology*, *72*, 91–100. https://doi.org/10.1016/j.conb.2021.09.009
2. Balch, W. E., Morimoto, R. I., Dillin, A., & Kelly, J. W. (2008). Adapting proteostasis for disease intervention. *Science (New York, N.Y.)*, *319*(5865), 916–919. https://doi.org/10.1126/science.1141448
3. Bays, N. W., Gardner, R. G., Seelig, L. P., Joazeiro, C. A., & Hampton, R. Y. (2001). Hrd1p/Der3p is a membrane-anchored ubiquitin ligase required for ER-associated degradation. *Nature Cell Biology*, *3*(1), 24–29. https://doi.org/10.1038/35050524
4. Bazopoulou, D., Knoefler, D., Zheng, Y., Ulrich, K., Oleson, B. J., Xie, L., Kim, M., Kaufmann, A., Lee, Y.-T., Dou, Y., Chen, Y., Quan, S., & Jakob, U. (2019). Developmental ROS individualizes organismal stress resistance and lifespan. *Nature*, *576*(7786), 301–305. https://doi.org/10.1038/s41586-019-1814-y
5. Bradner, J. E., West, N., Grachan, M. L., Greenberg, E. F., Haggarty, S. J., Warnow, T., & Mazitschek, R. (2010). Chemical phylogenetics of histone deacetylases. *Nature Chemical Biology*, *6*(3), 238–243. https://doi.org/10.1038/nchembio.313
6. Brenner, S. (1974). The genetics of Caenorhabditis elegans. *Genetics*, *77*(1), 71–94. https://doi.org/10.1093/genetics/77.1.71
7. Choong, C.-J., Sasaki, T., Hayakawa, H., Yasuda, T., Baba, K., Hirata, Y., Uesato, S., & Mochizuki, H. (2016). A novel histone deacetylase 1 and 2 isoform-specific inhibitor alleviates experimental Parkinson's disease. *Neurobiology of Aging*, *37*, 103–116. https://doi.org/10.1016/j.neurobiolaging.2015.10.001
8. Chou, C.-C., Vest, R., Prado, M. A., Wilson-Grady, J., Paulo, J. A., Shibuya, Y., Moran-Losada, P., Lee, T.-T., Luo, J., Gygi, S. P., Kelly, J. W., Finley, D., Wernig, M., Wyss-Coray, T., & Frydman, J. (2023). Proteostasis and lysosomal quality control deficits in Alzheimer's disease neurons. *bioRxiv: The Preprint Server for Biology*, 2023.03.27.534444. https://doi.org/10.1101/2023.03.27.534444
9. Christianson, J. C., Jarosch, E., & Sommer, T. (2023). Mechanisms of substrate processing during ER-associated protein degradation. *Nature Reviews. Molecular Cell Biology*, *24*(11), 777–796. https://doi.org/10.1038/s41580-023-00633-8
10. Chung, C. Y., Khurana, V., Auluck, P. K., Tardiff, D. F., Mazzulli, J. R., Soldner, F., Baru, V., Lou, Y., Freyzon, Y., Cho, S., Mungenast, A. E., Muffat, J., Mitalipova, M., Pluth, M. D., Jui, N. T., Schüle, B., Lippard, S. J., Tsai, L.-H., Krainc, D., … Lindquist, S. (2013). Identification and rescue of α-synuclein toxicity in Parkinson patient-derived neurons. *Science (New York, N.Y.)*, *342*(6161), 983–987. https://doi.org/10.1126/science.1245296
11. Costanzo, M., Baryshnikova, A., Bellay, J., Kim, Y., Spear, E. D., Sevier, C. S., Ding, H., Koh, J. L. Y., Toufighi, K., Mostafavi, S., Prinz, J., St Onge, R. P., VanderSluis, B., Makhnevych, T., Vizeacoumar, F. J., Alizadeh, S., Bahr, S., Brost, R. L., Chen, Y., … Boone, C. (2010). The genetic landscape of a cell.

Science (New York, N.Y.), *327*(5964), 425–431.
https://doi.org/10.1126/science.1180823

12. Couillault, C., Pujol, N., Reboul, J., Sabatier, L., Guichou, J.-F., Kohara, Y., & Ewbank, J. J. (2004). TLR-independent control of innate immunity in Caenorhabditis elegans by the TIR domain adaptor protein TIR-1, an ortholog of human SARM. *Nature Immunology*, *5*(5), 488–494. https://doi.org/10.1038/ni1060

13. Daniele, J. R., Higuchi-Sanabria, R., Durieux, J., Monshietehadi, S., Ramachandran, V., Tronnes, S. U., Kelet, N., Sanchez, M., Metcalf, M. G., Garcia, G., Frankino, P. A., Benitez, C., Zeng, M., Esping, D. J., Joe, L., & Dillin, A. (2020). UPRER promotes lipophagy independent of chaperones to extend life span. *Science Advances*, *6*(1), eaaz1441. https://doi.org/10.1126/sciadv.aaz1441

14. Davidson, K., & Pickering, A. M. (2023). The proteasome: A key modulator of nervous system function, brain aging, and neurodegenerative disease. *Frontiers in Cell and Developmental Biology*, *11*, 1124907. https://doi.org/10.3389/fcell.2023.1124907

15. Davis, M. W., Hammarlund, M., Harrach, T., Hullett, P., Olsen, S., & Jorgensen, E. M. (2005). Rapid single nucleotide polymorphism mapping in C. elegans. *BMC Genomics*, *6*, 118. https://doi.org/10.1186/1471-2164-6-118

16. Eesmaa, A., Yu, L.-Y., Göös, H., Nõges, K., Kovaleva, V., Hellman, M., Zimmermann, R., Jung, M., Permi, P., Varjosalo, M., Lindholm, P., & Saarma, M. (2021). The cytoprotective protein MANF promotes neuronal survival independently from its role as a GRP78 cofactor. *The Journal of Biological Chemistry*, *296*, 100295. https://doi.org/10.1016/j.jbc.2021.100295

17. Eichel, K., Uenaka, T., Belapurkar, V., Lu, R., Cheng, S., Pak, J. S., Taylor, C. A., Südhof, T. C., Malenka, R., Wernig, M., Özkan, E., Perrais, D., & Shen, K. (2022). Endocytosis in the axon initial segment maintains neuronal polarity. *Nature*, *609*(7925), 128–135. https://doi.org/10.1038/s41586-022-05074-5

18. Ge, S. X., Son, E. W., & Yao, R. (2018). iDEP: An integrated web application for differential expression and pathway analysis of RNA-Seq data. *BMC Bioinformatics*, *19*(1), 534. https://doi.org/10.1186/s12859-018-2486-6

19. Gerdts, J., Brace, E. J., Sasaki, Y., DiAntonio, A., & Milbrandt, J. (2015). SARM1 activation triggers axon degeneration locally via NAD$^+$ destruction. *Science (New York, N.Y.)*, *348*(6233), 453–457. https://doi.org/10.1126/science.1258366

20. Gerdts, J., Summers, D. W., Sasaki, Y., DiAntonio, A., & Milbrandt, J. (2013). Sarm1-mediated axon degeneration requires both SAM and TIR interactions. *The Journal of Neuroscience: The Official Journal of the Society for Neuroscience*, *33*(33), 13569–13580. https://doi.org/10.1523/JNEUROSCI.1197-13.2013

21. Guan, J.-S., Haggarty, S. J., Giacometti, E., Dannenberg, J.-H., Joseph, N., Gao, J., Nieland, T. J. F., Zhou, Y., Wang, X., Mazitschek, R., Bradner, J. E., DePinho, R. A., Jaenisch, R., & Tsai, L.-H. (2009). HDAC2 negatively regulates memory formation and synaptic plasticity. *Nature*, *459*(7243), 55–60. https://doi.org/10.1038/nature07925

22. Hanus, C., & Ehlers, M. D. (2016). Specialization of biosynthetic membrane trafficking for neuronal form and function. *Current Opinion in Neurobiology*, *39*, 8–16. https://doi.org/10.1016/j.conb.2016.03.004

23. Heiman, M. G., & Bülow, H. E. (2024). Dendrite morphogenesis in Caenorhabditis elegans. *Genetics*, *227*(2), iyae056. https://doi.org/10.1093/genetics/iyae056

24. Hetz, C., & Saxena, S. (2017). ER stress and the unfolded protein response in neurodegeneration. *Nature Reviews. Neurology*, *13*(8), 477–491. https://doi.org/10.1038/nrneurol.2017.99

25. Hoozemans, J. J. M., van Haastert, E. S., Nijholt, D. A. T., Rozemuller, A. J. M., Eikelenboom, P., & Scheper, W. (2009). The unfolded protein response is activated in pretangle neurons in Alzheimer's disease hippocampus. *The American Journal of Pathology*, *174*(4), 1241–1251. https://doi.org/10.2353/ajpath.2009.080814

26. Hubbert, C., Guardiola, A., Shao, R., Kawaguchi, Y., Ito, A., Nixon, A., Yoshida, M., Wang, X.-F., & Yao, T.-P. (2002). HDAC6 is a microtubule-associated deacetylase. *Nature*, *417*(6887), 455–458. https://doi.org/10.1038/417455a

27. Janczura, K. J., Volmar, C.-H., Sartor, G. C., Rao, S. J., Ricciardi, N. R., Lambert, G., Brothers, S. P., & Wahlestedt, C. (2018). Inhibition of HDAC3 reverses Alzheimer's disease-related pathologies in vitro and in the 3xTg-AD mouse model. *Proceedings of the National Academy of Sciences of the United States of America*, *115*(47), E11148–E11157. https://doi.org/10.1073/pnas.1805436115

28. Kurtishi, A., Rosen, B., Patil, K. S., Alves, G. W., & Møller, S. G. (2019). Cellular Proteostasis in Neurodegeneration. *Molecular Neurobiology*, *56*(5), 3676–3689. https://doi.org/10.1007/s12035-018-1334-z

29. Lindahl, M., Saarma, M., & Lindholm, P. (2017). Unconventional neurotrophic factors CDNF and MANF: Structure, physiological functions and therapeutic potential. *Neurobiology of Disease*, *97*(Pt B), 90–102. https://doi.org/10.1016/j.nbd.2016.07.009

30. Lippincott-Schwartz, J., Roberts, T. H., & Hirschberg, K. (2000). Secretory protein trafficking and organelle dynamics in living cells. *Annual Review of Cell and Developmental Biology*, *16*, 557–589. https://doi.org/10.1146/annurev.cellbio.16.1.557

31. Liu, C.-L., Zhong, W., He, Y.-Y., Li, X., Li, S., & He, K.-L. (2016). Genome-wide analysis of tunicamycin-induced endoplasmic reticulum stress response and the protective effect of endoplasmic reticulum inhibitors in neonatal rat cardiomyocytes. *Molecular and Cellular Biochemistry*, *413*(1–2), 57–67. https://doi.org/10.1007/s11010-015-2639-0

32. Liu, O. W., & Shen, K. (2011). The transmembrane LRR protein DMA-1 promotes dendrite branching and growth in C. elegans. *Nature Neuroscience*, *15*(1), 57–63. https://doi.org/10.1038/nn.2978

33. Lu, T., Aron, L., Zullo, J., Pan, Y., Kim, H., Chen, Y., Yang, T.-H., Kim, H.-M., Drake, D., Liu, X. S., Bennett, D. A., Colaiácovo, M. P., & Yankner, B. A. (2014). REST and stress resistance in ageing and Alzheimer's disease. *Nature*, *507*(7493), 448–454. https://doi.org/10.1038/nature13163

34. Mai, A., Rotili, D., Valente, S., & Kazantsev, A. G. (2009). Histone deacetylase inhibitors and neurodegenerative disorders: Holding the promise. *Current Pharmaceutical Design*, *15*(34), 3940–3957. https://doi.org/10.2174/138161209789649349

35. Maor-Nof, M., Homma, N., Raanan, C., Nof, A., Hirokawa, N., & Yaron, A. (2013). Axonal pruning is actively regulated by the microtubule-destabilizing protein kinesin superfamily protein 2A. *Cell Reports*, *3*(4), 971–977. https://doi.org/10.1016/j.celrep.2013.03.005

36. McCampbell, A., Taye, A. A., Whitty, L., Penney, E., Steffan, J. S., & Fischbeck, K. H. (2001). Histone deacetylase inhibitors reduce polyglutamine toxicity. *Proceedings of the National Academy of Sciences of the United States of America*, *98*(26), 15179–15184. https://doi.org/10.1073/pnas.261400698

37. Neukomm, L. J., Burdett, T. C., Seeds, A. M., Hampel, S., Coutinho-Budd, J. C., Farley, J. E., Wong, J., Karadeniz, Y. B., Osterloh, J. M., Sheehan, A. E., & Freeman, M. R. (2017). Axon Death Pathways Converge on Axundead to Promote Functional and Structural Axon Disassembly. *Neuron*, *95*(1), 78-91.e5. https://doi.org/10.1016/j.neuron.2017.06.031

38. Nijholt, D. A. T., van Haastert, E. S., Rozemuller, A. J. M., Scheper, W., & Hoozemans, J. J. M. (2012). The unfolded protein response is associated with early tau pathology in the hippocampus of tauopathies. *The Journal of Pathology*, *226*(5), 693–702. https://doi.org/10.1002/path.3969

39. Oleson, B. J., Bhattrai, J., Zalubas, S. L., Kravchenko, T. R., Ji, Y., Jiang, E. L., Lu, C. C., Madden, C. R., Coffman, J. G., Bazopoulou, D., Jones, J. W., & Jakob, U. (2024). Early life changes in histone landscape protect against age-associated amyloid toxicities through HSF-1-dependent regulation of lipid metabolism. *Nature Aging*, *4*(1), 48–61. https://doi.org/10.1038/s43587-023-00537-4

40. Oslowski, C. M., & Urano, F. (2011). Measuring ER stress and the unfolded protein response using mammalian tissue culture system. *Methods in Enzymology*, *490*, 71–92. https://doi.org/10.1016/B978-0-12-385114-7.00004-0

41. Osterloh, J. M., Yang, J., Rooney, T. M., Fox, A. N., Adalbert, R., Powell, E. H., Sheehan, A. E., Avery, M. A., Hackett, R., Logan, M. A., MacDonald, J. M., Ziegenfuss, J. S., Milde, S., Hou, Y.-J., Nathan, C., Ding, A., Brown, R. H., Conforti, L., Coleman, M., … Freeman, M. R. (2012). dSarm/Sarm1 is required for activation of an injury-induced axon death pathway. *Science (New York, N.Y.)*, *337*(6093), 481–484. https://doi.org/10.1126/science.1223899

42. Outeiro, T. F., Kontopoulos, E., Altmann, S. M., Kufareva, I., Strathearn, K. E., Amore, A. M., Volk, C. B., Maxwell, M. M., Rochet, J.-C., McLean, P. J., Young, A. B., Abagyan, R., Feany, M. B., Hyman, B. T., & Kazantsev, A. G. (2007). Sirtuin 2 inhibitors rescue alpha-synuclein-mediated toxicity in models of Parkinson's disease. *Science (New York, N.Y.)*, *317*(5837), 516–519. https://doi.org/10.1126/science.1143780

43. Petrova, P., Raibekas, A., Pevsner, J., Vigo, N., Anafi, M., Moore, M. K., Peaire, A. E., Shridhar, V., Smith, D. I., Kelly, J., Durocher, Y., & Commissiong, J. W. (2003). MANF: A new mesencephalic, astrocyte-derived neurotrophic factor with selectivity for dopaminergic neurons. *Journal of Molecular Neuroscience: MN*, *20*(2), 173–188. https://doi.org/10.1385/jmn:20:2:173

44. Rivieccio, M. A., Brochier, C., Willis, D. E., Walker, B. A., D'Annibale, M. A., McLaughlin, K., Siddiq, A., Kozikowski, A. P., Jaffrey, S. R., Twiss, J. L., Ratan, R. R., & Langley, B. (2009). HDAC6 is a target for protection and regeneration following injury in the nervous system. *Proceedings of the National Academy of Sciences of the United States of America*, *106*(46), 19599–19604. https://doi.org/10.1073/pnas.0907935106

45. Robert, V. J., Caron, M., Gely, L., Adrait, A., Pakulska, V., Couté, Y., Chevalier, M., Riedel, C. G., Bedet, C., & Palladino, F. (2023). SIN-3 acts in distinct complexes to regulate the germline transcriptional program in Caenorhabditis elegans. *Development (Cambridge, England)*, *150*(21), dev201755. https://doi.org/10.1242/dev.201755

46. Salzberg, Y., Coleman, A. J., Celestrin, K., Cohen-Berkman, M., Biederer, T., Henis-Korenblit, S., & Bülow, H. E. (2017). Reduced Insulin/Insulin-Like Growth Factor Receptor Signaling Mitigates Defective Dendrite Morphogenesis in Mutants of the ER Stress Sensor IRE-1. *PLoS Genetics*, *13*(1), e1006579. https://doi.org/10.1371/journal.pgen.1006579

47. Sambashivan, S., & Freeman, M. R. (2021). SARM1 signaling mechanisms in the injured nervous system. *Current Opinion in Neurobiology*, *69*, 247–255. https://doi.org/10.1016/j.conb.2021.05.004

48. Seto, E., & Yoshida, M. (2014). Erasers of histone acetylation: The histone deacetylase enzymes. *Cold Spring Harbor Perspectives in Biology*, *6*(4), a018713. https://doi.org/10.1101/cshperspect.a018713

49. Shi, R., Ho, X. Y., Tao, L., Taylor, C. A., Zhao, T., Zou, W., Lizzappi, M., Eichel, K., & Shen, K. (2024). Stochastic growth and selective stabilization generate stereotyped dendritic arbors. *bioRxiv: The Preprint Server for Biology*, 2024.05.08.591205. https://doi.org/10.1101/2024.05.08.591205

50. Shukla, S., & Tekwani, B. L. (2020). Histone Deacetylases Inhibitors in Neurodegenerative Diseases, Neuroprotection and Neuronal Differentiation. *Frontiers in Pharmacology*, *11*, 537. https://doi.org/10.3389/fphar.2020.00537

51. Singh, R., Kaur, N., Choubey, V., Dhingra, N., & Kaur, T. (2024). Endoplasmic reticulum stress and its role in various neurodegenerative diseases. *Brain Research*, *1826*, 148742. https://doi.org/10.1016/j.brainres.2023.148742

52. Smith, C. J., Watson, J. D., Spencer, W. C., O'Brien, T., Cha, B., Albeg, A., Treinin, M., & Miller, D. M. (2010). Time-lapse imaging and cell-specific expression profiling reveal dynamic branching and molecular determinants of a multi-dendritic nociceptor in C. elegans. *Developmental Biology*, *345*(1), 18–33. https://doi.org/10.1016/j.ydbio.2010.05.502

53. Sontag, E. M., Samant, R. S., & Frydman, J. (2017). Mechanisms and Functions of Spatial Protein Quality Control. *Annual Review of Biochemistry*, *86*, 97–122. https://doi.org/10.1146/annurev-biochem-060815-014616

54. Suelves, N., Kirkham-McCarthy, L., Lahue, R. S., & Ginés, S. (2017). A selective inhibitor of histone deacetylase 3 prevents cognitive deficits and suppresses striatal CAG repeat expansions in Huntington's disease mice. *Scientific Reports*, *7*(1), 6082. https://doi.org/10.1038/s41598-017-05125-2

55. Sulston, J. E., & Horvitz, H. R. (1977). Post-embryonic cell lineages of the nematode, Caenorhabditis elegans. *Developmental Biology*, *56*(1), 110–156. https://doi.org/10.1016/0012-1606(77)90158-0

56. Tan, L., Shi, J., Moghadami, S., Parasar, B., Wright, C. P., Seo, Y., Vallejo, K., Cobos, I., Duncan, L., Chen, R., & Deisseroth, K. (2023). Lifelong restructuring of 3D genome architecture in cerebellar granule cells. *Science (New York, N.Y.)*, *381*(6662), 1112–1119. https://doi.org/10.1126/science.adh3253

57. Taylor, C. A., Yan, J., Howell, A. S., Dong, X., & Shen, K. (2015). RAB-10 Regulates Dendritic Branching by Balancing Dendritic Transport. *PLoS Genetics*, *11*(12), e1005695. https://doi.org/10.1371/journal.pgen.1005695

58. Thibault, G., Ismail, N., & Ng, D. T. W. (2011). The unfolded protein response supports cellular robustness as a broad-spectrum compensatory pathway. *Proceedings of the National Academy of Sciences of the United States of America*, *108*(51), 20597–20602. https://doi.org/10.1073/pnas.1117184109

59. Tian, Y., Garcia, G., Bian, Q., Steffen, K. K., Joe, L., Wolff, S., Meyer, B. J., & Dillin, A. (2016). Mitochondrial Stress Induces Chromatin Reorganization to Promote Longevity and UPR(mt). *Cell*, *165*(5), 1197–1208. https://doi.org/10.1016/j.cell.2016.04.011

60. Tsalik, E. L., Niacaris, T., Wenick, A. S., Pau, K., Avery, L., & Hobert, O. (2003). LIM homeobox gene-dependent expression of biogenic amine receptors in restricted regions of the C. elegans nervous system. *Developmental Biology*, *263*(1), 81–102. https://doi.org/10.1016/s0012-1606(03)00447-0

61. Way, J. C., & Chalfie, M. (1989). The mec-3 gene of Caenorhabditis elegans requires its own product for maintained expression and is expressed in three neuronal cell types. *Genes & Development*, *3*(12A), 1823–1833. https://doi.org/10.1101/gad.3.12a.1823

62. Wei, X., Howell, A. S., Dong, X., Taylor, C. A., Cooper, R. C., Zhang, J., Zou, W., Sherwood, D. R., & Shen, K. (2015). The unfolded protein response is required for dendrite morphogenesis. *eLife*, *4*, e06963. https://doi.org/10.7554/eLife.06963

63. Winckler, B., Faundez, V., Maday, S., Cai, Q., Guimas Almeida, C., & Zhang, H. (2018). The Endolysosomal System and Proteostasis: From Development to Degeneration. *The Journal of Neuroscience: The Official Journal of the Society for Neuroscience*, *38*(44), 9364–9374. https://doi.org/10.1523/JNEUROSCI.1665-18.2018

64. Wiseman, R. L., Mesgarzadeh, J. S., & Hendershot, L. M. (2022). Reshaping endoplasmic reticulum quality control through the unfolded protein response. *Molecular Cell*, *82*(8), 1477–1491. https://doi.org/10.1016/j.molcel.2022.03.025

65. Zou, W., Yadav, S., DeVault, L., Nung Jan, Y., & Sherwood, D. R. (2015). RAB-10-Dependent Membrane Transport Is Required for Dendrite Arborization. *PLoS Genetics*, *11*(9), e1005484. https://doi.org/10.1371/journal.pgen.1005484

66. Zullo, J. M., Drake, D., Aron, L., O'Hern, P., Dhamne, S. C., Davidsohn, N., Mao, C.-A., Klein, W. H., Rotenberg, A., Bennett, D. A., Church, G. M., Colaiácovo, M. P., & Yankner, B. A. (2019). Regulation of lifespan by neural excitation and REST. *Nature*, *574*(7778), 359–364. https://doi.org/10.1038/s41586-019-1647-8